# CO$_2$ Capture by Potassium Carbonate Nanocomposites

## February 2016

Chiba University

Graduate School of Science

Division of Fundamental Sciences

Department of Chemistry

Guang Yang

# Contents

**Chapter 3: $CO_2$ capture by carbon aerogel–potassium**

**carbonate nanocomposites** ................................... 39

# Chapter 1: General introduction

Greenhouse gases (GHGs) consist of ten primate components, perfluorocarbons ($CF_4$, $C_2F_6$), hydrofluorocarbon ($CHF_3$, $CF_3CH_2F$, $CH_3CHF_2$), and sulfur hexafluoride ($SF_6$) result from industrial processes. Even though the concentration is increased after pre-industrial, the increment is little and does not play an important role in environment changes. However water vapor ($H_2O$), carbon dioxide ($CO_2$), methane ($CH_4$) and nitrous oxide ($N_2O$) have increased greatly due to the human activity in recent years. Carbon dioxide is a principal anthropogenic greenhouse, most of the huge amounts of $CO_2$ come from the emission of power plants, gas processing industries, petrochemical industries, iron and steel industries, cement industries [1, 2] and 44% of $CO_2$ emission come from the combustion of fossil fuels [3], which contribute to global warming and anthropogenic climate change. Between 1750 and 1998, the concentration of $CO_2$ in the atmosphere had increased from 280 ppm to 380 ppm [4-7], and is expected to reach 550 ppm by 2050. It has been anticipated that in 2100 (570 ppm) the average global temperature will increase 5.8℃, and sea level will rise by 0.88 m [8], melt polar caps (average arctic sea ice has shrunk by 2.7% per decade) [9] and other environment issues such as droughts, deserts, permafrost melt, inundation, sea level rise, and ecosystem disruption will significantly affect the survival of mankind.

Fossil fuels still will be the main energy resources in the next decades, due to its large current greenhouse forcing, long persistence in the atmosphere and the advantage such as low cost, high energy density, availability, and feasible technology [8, 10]. Though

alternative energy has been investigated, none of them could meet global energy demands for the near future. Carbon capture and sequestration (CCS) produce a concentrated stream of $CO_2$ at a high pressure and transported readily to a storage site which has been paid increasing attention to reduce levels of $CO_2$ in the atmosphere and at the same time fossil fuels can be used sequentially. The International Panel on Climate Change (IPCC) classified carbon capture and storage into three-stage strategy for migrating $CO_2$ emissions, involving 1) separation, 2) transportation, and 3) storage of $CO_2$ [11]. According to the report that warming will continue beyond 2100 due to the temperature will remain elevated constant levels even though after a complete $CO_2$ cessation except a large number $CO_2$ has been captured from the atmosphere [12], so capture and storage $CO_2$ is emergent. $CO_2$ can also be recognized as used as a renewable carbon source and industrial syntheses raw material, transforming to carboxylic acids, organic carbonates, urea, and methanol [13].

## 1.1 $CO_2$ capture and sequestration (CCS)
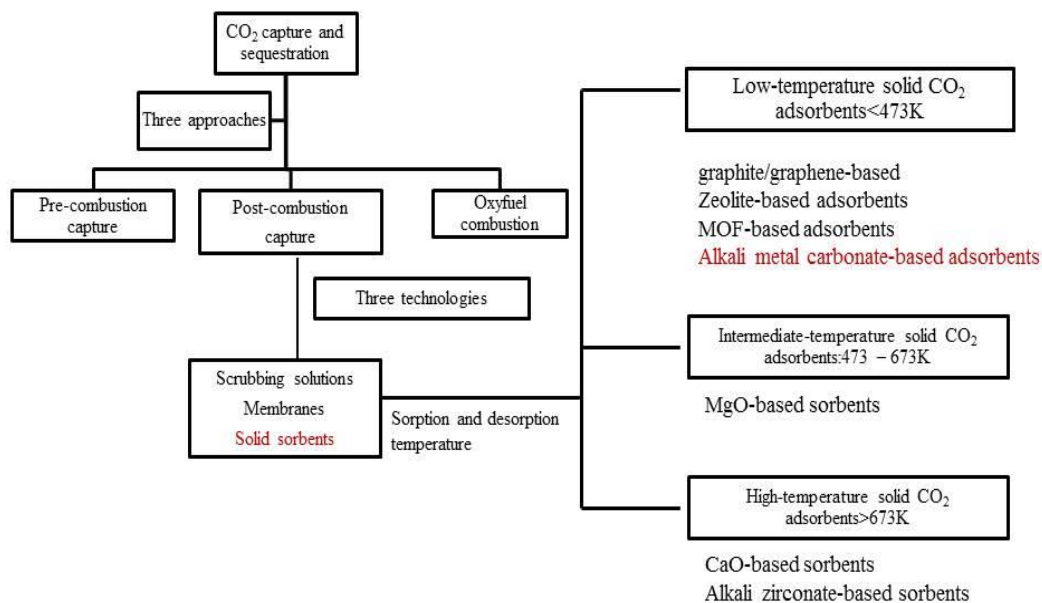


**Figure 1-1:** The approaches and technology of $CO_2$ capture and sequestration [14].

1.1.1 Three approaches of $CO_2$ capture

As showed in Figure1-1 there are three approaches to capture $CO_2$ from flue gas, divided into pre-combustion capture, post-combustion capture and oxyfuel combustion. Figure1-2 illustrates the detail processes of three approaches.

a) Pre-combustion capture is the reaction of fuel gas with oxygen or air and in some cases steam to produce synthesis gas which mainly composed of carbon monoxide and hydrogen, and the monoxide further reacted with steam to give carbon dioxide and more hydrogen. This system needs long term development to achieve targeted efficiency and this method involves $CO_2$ capture at high temperatures (527K-773K) accompanied by the production of hydrogen (water-gas shift reaction).

b) In contrast to pre-combustion, oxy-fuel combustion uses pure oxygen instead of ambient air. Even though this method could get high $CO_2$ concentration, capital cost is high and enormous energy would be consumed to separate oxygen from air. Oxy-fuel combustion can be applied to several fuels, consist of coal gas, natural gas or blends of biomass and coal [15].

c) Post-combustion capture is $CO_2$ separation and storage from flue gas after combustion. This system does not require expensive technologies (syngas separation, fuel cell) and can be used directly without change the combustion cycle. So post-combustion is the most important approach to mitigate $CO_2$ emissions [3, 16-18].
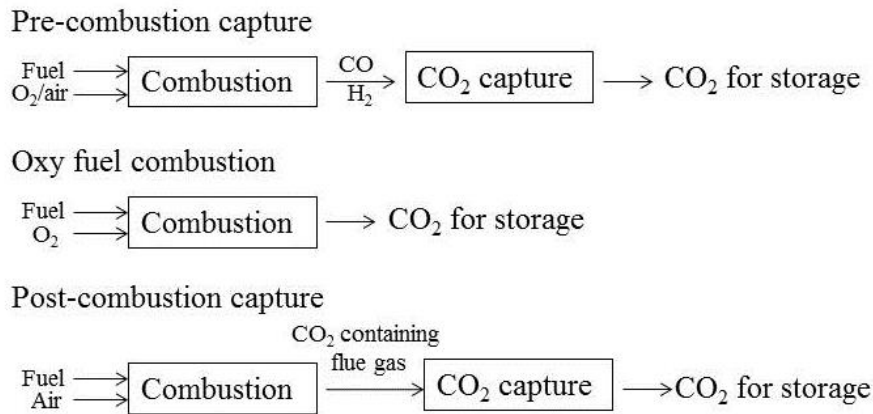
**Figure 1-2:** Three basic approaches of $CO_2$ capture [16]

1.1.2 Methods of $CO_2$ absorption

Carbon dioxide can be removed from flue gas by various methods, and three main technologies include scrubbing solution, membranes and solid sorbent. Currently amine scrubbing is the most available process for $CO_2$ adsorption, however this method presents several disadvantages, including the nature of corrosive, toxic emissions, limited stability, and high energy consumption in regeneration process inhibit the application [19]. Membrane separation method is a continuous, clean and simple process for $CO_2$ recovery, however the selectivity of $CO_2$ from NOx and SOx is very low, and it is not suitable for high flow rate application. This process has been conditioned by some factors such as, 1) high $CO_2$ permeability, 2) high selectivity for $CO_2$ separation from flue gases, 3) resistant to aging, 4) resistant to plasticization, and 5) low production cost for different membrane modules [2]. The details of solid sorbents will discuss in the next paragraph.

1.1.3 Classification of solid materials

Wang et al. organized solid sorbents into three types, according to their desorption

temperature [14].

(1) low-temperature sorbents, including graphite/graphene-based, zeolite-based, metal-organic frameworks (MOFs)-based, alkali metal carbonate-based adsorbents. (2) intermediate-temperature sorbents such as MgO-base sorbents, and (3) high-temperature sorbents like CaO-based sorbents. Among the various adsorbents dry alkali metal-based sorbents for capturing $CO_2$ is considered to be one of the most promising technologies because these sorbents can capture $CO_2$ at a suitable temperature (313-343 K) and also could be regenerated at an appropriate temperature below 473 K. However a process which is inexpensive, needs low energy demand, and has high $CO_2$ capture capacity is still under development.

## 1.2 The dry sorbents for $CO_2$ capture

The dry sorbents could be divided into alkaline earth metal-based sorbents which contribute to the following formula: $XO+CO_2 \rightleftarrows XCO_3$(X=Mg, Ca), and alkali metal-based sorbents which is described as: $M_2CO_3+H_2O+CO_2 \rightleftarrows 2HKCO_3$ (M=K, Na) [20]. Zhao et al. verified that $Na_2CO_3$ and $K_2CO_3$ are suitable to $CO_2$ capture under post-combustion conditions through the phonon density of states calculations among $M_2CO_3$, $M_2O$, and MOH (M=K, Na) phase [21].

1.2.1 Alkaline earth metal-based sorbents

Solid metal oxide can be used as $CO_2$ capture material, the mechanism is presented as follows [22].

$$MO+CO_2 \rightarrow MCO_3 \qquad (1-1)$$

$$MCO_3 \rightarrow MO+CO_2 \qquad (1-2)$$

The forward step (1-1) describe the carbonation reaction that solid metal oxide reacts

with $CO_2$ gaseous, and when the temperature rising beyond the calcination temperature, occurring the reverse reaction (1-2). Solid metal oxides present tremendous advantages such as directly react with $CO_2$ under flue gas condition (393 K-1073 K), providing high equilibrium capacities and producing high purity $CO_2$ streams. However, the maximum carbonation conversion of $CaCO_3$ is decreased quickly with the increasing regeneration cycles due to the sintering from high calcination temperature. Cupta et al. summarized calcination temperature of various solid metal oxides, investigated CaO from different precursor and found the introduction of mesoporous structure may lead to less susceptible to pore blocking and with a high conversation above 90%. However $CO_2$ capture capacity of CaO decreased rapidly during the looping process [23], in order to resolve this problem attapulgite had been doped to limestone, and optimal ratio of attapulgite was found to be 15 wt%, which increased $CO_2$ capture performance and greatly slowed down the decay during recyclability. Sun et al. [24] doped manganese salts to $CaCO_3$ and found through the modification could get a better carbonation rate and enhance the calcination/carbonation cycles. There have tremendous investigation such as thermal pretreatment, acetic acid modification, doping with $KMnO_4$ used to enhance $CO_2$ capture capacity and optimize the recyclability [25-27].

1.2.2 Alkali-metal carbonate sorbents

Capture $CO_2$ from an actual flue gas mixture which has a significant amount of $H_2O$ is one of the most difficult processes at present. Moisture usually contains as high as 8-17% in the flue gases which could destroy the nanostructure and adversely affects the $CO_2$ capture capacity, so it is important to be removed before adsorption process to the conventional methods [28, 29]. Alkali metal carbonates such as $K_2CO_3$ and $Na_2CO_3$ can be used to capture $CO_2$ in the moist ambient at relatively low temperature. However

analytical reagent has a very low reaction rate, Liang et al. reported $Na_2CO_3$ converted to $NaHCO_3$ at 333 K and 343 K, required 200 min to attain the equilibrium value in a fixed-bed test [5]. The carbonation reaction was also slow for $K_2CO_3$ and carbonation conversion was only 45% in 100 min [30], however $K_2CO_3$ calcined from $KHCO_3$ which owned the hexagonal crystal structure possessed a relative high reaction rate and $CO_2$ capture capacity [8]. It had been extensively investigated the $CO_2$ capture capacity and kinetics of alkali metal sorbent, having a conclusion that $K_2CO_3$ is prior than $Na_2CO_3$ [4, 6, 31]. So in this research we used $K_2CO_3$ as the sorbents loaded on the carbon aerogel.

1.2.3 Effect of temperature on the carbonation
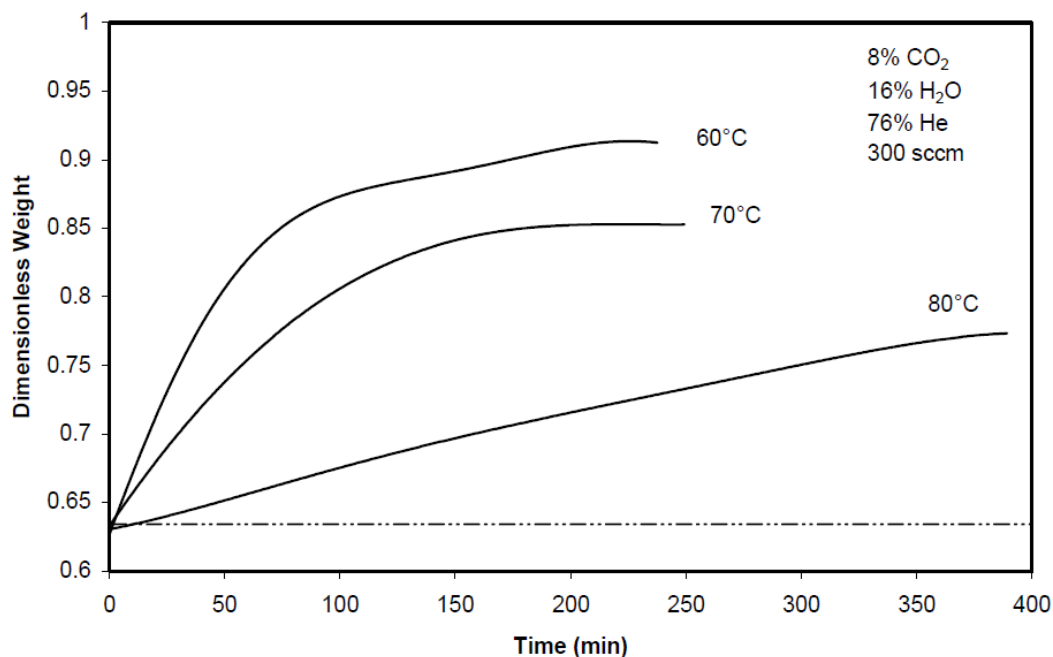


**Figure 1-3:** Effect of temperature on the carbonation [32]

It has been generally recognized that temperature control plays an important role in the carbonation reaction, which has a narrow range because of the dew point of fed gas

and thermodynamics of the reversible reaction. Green et al. summarized how temperature affected the carbonation process, as showed in Figure1-3. with the increase in temperature, there was a decrease in kinetics and thermodynamics in $CO_2$ capture, for 353K the reaction was still proceeding when reactive time beyond 400 min [32].

## 1.3 $K_2CO_3$-composites

There are many researches have been studied associate with impregnating $K_2CO_3$ on porous materials [33]. Zhao et al. compared the analytical-reagent samples of $K_2CO_3$, $K_2CO_3.1.5H_2O$, and $KHCO_3$ with loading them on activated carbon or $\gamma$-$Al_2CO_3$ respectively. It is concluded that the carbonation conversions increased due to combine analytical reagent with porous material [31]. Sevilla et al. [34] reported the relationship between the porous characteristics of the carbon sorbents and their capacity for $CO_2$ adsorption at 298K and 1 bar, the result showed that $CO_2$ capture capacity is principally due to the presence of narrow micropores. The nature of the support affected the $CO_2$ capture capacity of the sorbent, such as AC-$K_2CO_3$ sorbent possess a disadvantage that has to carry out the pretreatment process by water [20]. Zeolites possess appropriate pore structures for $CO_2$ adsorption, because of the same magnitude with $CO_2$ molecules [33], Silica aerogels(SG) have an open pore structure, a high surface area and low density, but through the $K_2CO_3$ loading process lead to completely collapsed of microscopic structure and $CO_2$ capture capacity decreased significantly [33, 35]. $K_2CO_3$ loaded with vermiculite which possessed a large pore size also without a high $CO_2$ capture capacity was caused by a lower dispersion of $K_2CO_3$ [36]. And MgO-$K_2CO_3$ sorbent could capture carbon dioxide at elevated temperature, after $CO_2$ absorption three phase had been detected which were $K_2CO_3$, MgO, and $K_2Mg(CO)_3$ instead of $KHCO_3$

8

and $MgCO_3$. They also reported that the best ratio of Mg to K is 1:3 and the optimal temperature for $CO_2$ capture is 648 K [37].

The morphological feature after $K_2CO_3$ loading is various highly depend on the properties like porous structure of support material, such as there was no obvious change in the surface area when loaded on carbon because $K_2CO_3$ was supported in macropores, on the contrary, $K_2CO_3$ loaded on silica gel resulted in a drastic decrease in the surface area because of hydrophilicity of silica surface, and impregnated $K_2CO_3$ in activated cokes lead to block the pore mouth and decrease the surface area [29, 38]. Zhao et al. investigated the active distribution behaviors of CA and $Al_2O_3$, and found they had different distribution because of the various properties of support. CA sorbents adsorbed $H_2O$ to turn into $K_2CO_3.1.5H_2O$, however, $Al_2O_3$ sorbents captured $H_2O$ in the pore at first and then react with $CO_2$ [31]. Just as above mentioned, a lot of researches about composites have been studied, however these sorbents all possessed disadvantage factors in $CO_2$ capture process, this study focus on the carbon aerogel which still not be investigated systematically.

## 1.4 Carbon aerogel

Carbon gels have been paid attention for many years, because carbon gels own large specific surface area, and could be readily tailored to appropriate pore structure for various application. The properties of pore structure rely not only on the initial conditions in the synthetic process but also on the drying method and carbonization techniques. According to drying techniques, carbon gels could be classified into a) carbon xerogel, b) carbon cryogel, and c) carbon aerogel [43, 44].

**a)** Carbon xerogel: the simplest way to convert the hydrogel into a solid gel by drying in an inert atmosphere, however xerogel have a more compact structure than others and display the lowest surface area and pore volume.

**b)** Carbon cryogel: RF hydrogel are lyophilized free-drying in t-butanol solvent. The value change of t-butanol is much smaller than water in the freezing process. And this process is less expensive and can generate high surface area carbon with easily tailored pore structure. The surface area is higher than the aerogel which is dried under supercritical conditions even the drying shrinkage of the cryogel is a litter larger than the aerogel, however the surface area decrease with time result from instability of intrinsic structural modification [45].

**c)** Carbon aerogel: supercritical drying with carbon dioxide. Even though this technique is expensive, carbon aerogel is an effective way of obtaining mesoporous RF gels. In the extraction step the temperature and drying time modify the total porosity, Czakkel et al. [46] reported that under 313 K, 80 bar the phase is homogeneous if $CO_2$ alone is present, and the higher pressures prefer to greater macroporosity, drying time affects the total pore volume. The difference between liquid and super supercritical $CO_2$ extraction also had been interpreted, verifying there was no shrinkage by using supercritical $CO_2$.

Base on the interpretation above we chose carbon aerogel to be the matrix, because of the high surface area and stability with time. There are still other factors affect the final structure of carbon aerogel, such as the nature of the catalyst, pH in the synthesis step, temperature, molar ratios and total concentration. The pH values play an important role on gelation time and primary particles size which affects the final properties of the aerogel. When pH smaller than 0.8, the reactants will lead to precipitation, in the range of 1 to 4 of pH could promote viable gel formation and reduce gelation times. pH 5.5 to

7.5 is the most suitable region for synthesizing RF gel, and once the pH is higher than 7.5, there will no porous in the final structure.

D.Faire'n-Jime'nez et al. [41] investigated different catalysts such as alkaline carbonates and acidic catalysts affected the final pore texture in the polycondensation reaction, and found the density of RF gel samples had the order as follow: Acid catalysts $> Na_2CO_3 > K_2CO_3$, and in the acidic conditions usually got two or three fold higher than basic conditions gave rise to the conclusion that a denser solution would generate smaller pore volume and narrow pore sizes distribution. Shaheen A.Al-Muhtaseb et al. [42] reported a review about the effects of synthesis and processing conditions to the final nanostructure of carbon aerogel and carbon xerogel. The variation of concentration ratios also has an important influence in changing the structure properties. Taylor et al. verified that high ratio of R/C would lower the cluster number concentration and longer the gelation time, ultimately generate larger pore size, vice versa.

Figure1-4 shows the process of carbon aerogel. Resorcinol (1, 3-dihydroxybenzene, $C_6H_4 (OH)_2$) and formaldehyde (HCHO) RF sol-gels have been synthesized by Pekala and co-workers, usually the process could be classified into two steps, after the formation of hydroxymethyl derivatives ($-CH_2OH$) of resorcinol, the intermediate products will condensed to form methylene ($-CH_2-$) and methylene-ether ($-CH_2OCH_2-$) bridged compounds. A three-dimensional polymer matrix (RF hydrogel) is formed, and through the solvent exchange, drying treatment, carbonation, we can get a solid carbon skeleton [9, 39, 40].

Step 1: Addition reaction
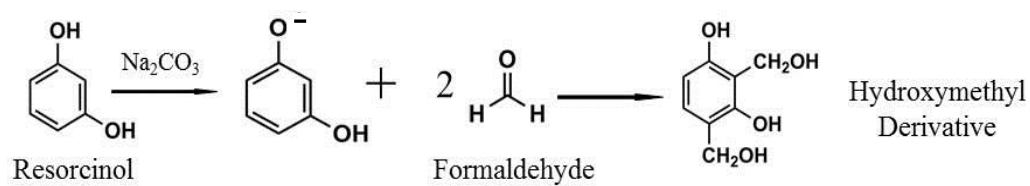


Step 2: Condensation reaction
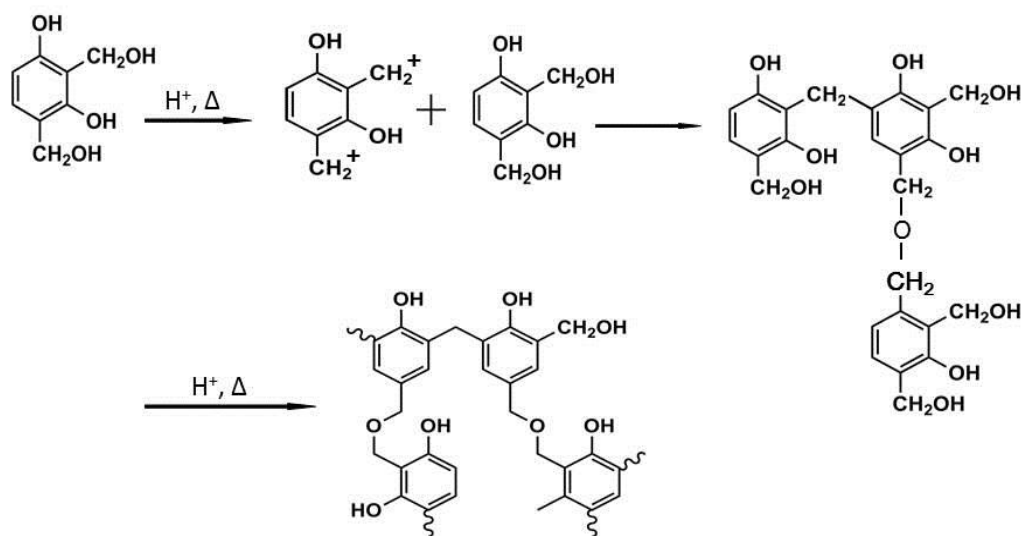


**Figure1-4:** Reaction mechanism of the sol-gel polymerization of resorcinol with formaldehyde [48].

# References

[1] S－Y. Lee, S－J Park, Determination of the optimal pore size for improved $CO_2$ adsorption in activated carbon fibers, Journal of Colloid and Interface Science, 2003, 389, 230-235.

[2] M. Songolzadeh, M. Soleimani, M. T. Ravanchi, R. Songolzadeh, Carbon dioxide separation from flue gases: A technological review emphasizing reduction in greenhouse gas emissions, the Scientific World Journal, Article ID 828131, 2014, 34 pages.

[3] J. Wang, A. Heerwig, M. R. Lohe, M. Oschatz, L. Borchardt, S. Kaskel, Fungi-based porous carbons for $CO_2$ adsorption and separation, Journal of Materials Chemistry, 2012, 22, 13911-13913.

[4] S－W. Park, D－H Sung, B－S. Choi, J－W. Lee, H. Kumazawa, Carbonation Kinetics of potassium carbonate by carbon dioxide, Journal of Industrial and Engineering Chemistry, 2006, 12(4), 522-530.

[5] Y. Liang, D. P. Harrison, Carbon dioxide capture using dry sodium-based sorbents, Energy &Fuels, 2004, 18(2),569-575.

[6] S－W Park, D－H Sung, B－S Choi, K-J. Oh, K－H Moon, Sorption of carbon dioxide onto sodium carbonate, Separation Science and Technology, 2006, 41(12), 2665-2684.

[7] D. A. Green, B. S. Turk, R. P. Gupta, W. J. McMichael, D. P. Harrison, Y. Liang, Carbon dioxide capture from flue gas using dry regenerable sorbents, Quarterly Technical Process Report; Research Triangle Institute: Research Triangle Park, NC, April 2002.

[8] C. Zhao, X. Chen, C. Zhao, Y. Liu, Carbonation and hydration characteristics of dry Potassium-Based Sorbents for $CO_2$ Capture, Energy & Fuels, 2009, 23, 1766-1769.

[9] C−W Moon, Y. Kim, S−S Im, S−J. Park, Effect of activation temperature on $CO_2$ capture behaviors of resorcinol-based carbon aerogels, Bulletin of Korean Chemical Society, 2014, 35(1), 57-61.

[10] L.K.C.de Souza, N. P. Wickramaratne, A. S. Ello, M. J. F. Costa, C. E. F. da Costa, M. Jaroniec, Enhancement of $CO_2$ adsorption on phenolic resin-based mesoporous carbons by KOH activation, Carbon , 2013, 65, 334-340.

[11] B. Metz, O. Davidson , H. Coninck ,M. Loos, L. Meyer, IPCC special report on carbon dioxide capture and storage, Cambridge, UK, 2005.

[12] IPCC, 2014: Climate Change 2014: Synthesis Report. Contribution of working groups Ⅰ,Ⅱ,and Ⅲ to the Fifth Assessment Report of the Intergovernmental Panel on Climate Change. IPCC, Geneva, Switzerland, 151.

[13] M. Mikkelsen, M. Jorgensen, F. C. Krebs, The teraton challenge, A review of fixation and transformation of carbon dioxide. Energy & Environmental Science, 2010, 3, 43-81.

[14] J. Wang, L. Huang, R. Yang, Z. Zhang, J. Wu, Y. Gao, Q. Wang, D. Hare, Z. Zhong, Recent advances in solid sorbents for $CO_2$ capture and new development trends, Energy & Environmental Science, 2014, 7, 3478-3518.

[15] M. E. Boot-Handford, J. C. Abanades, E. J. Anthony, M. J. Blunt, S. Brandani, N. M. Dowell et al., Carbon capture and storage update, Energy & Environmental Science , 2014, 7, 130-189.

[16] R. Thiruvenkatachari, S. Su, H. An, X. X. Yu, Post combustion $CO_2$ capture by carbon fibre monolithic adsorbents, Progress in energy and combustion science, 2009, 35, 438-455.

[17] E. Rubin, H.de Coninck, IPCC special report on carbon dioxide capture and storage,

Tech. Rep., Cambridge University Press, UK, 2005, TNO, Cost Curves for $CO_2$ Storage, part 2, 2004.

[18] T. F. Wall, Combustion processes for carbon capture, Proceedings of the combustion institute, 2007, 31, 31-44.

[19] N. A. H. Meis, A. M. Frey, J. H. Bitter, K. P. de Jong, Carbon Nanofiber-Supported $K_2CO_3$ as an efficient Low-Temperature regenerable $CO_2$ sorbent for post-combustion capture, Industrial & Engineering Chemistry Research, 2013, 52, 12812-12818.

[20] S. C. Lee, J. C. Kim, Dry potassium-based sorbents for $CO_2$ capture, Catalysis Surveys from Asia, 2007, 11, 171-185.

[21] C. Zhao, X. Chen, E. J. Anthony, X. Jiang, L. Duan, Y. Wu, W. Dong, C. Zhao, Capturing $CO_2$ in flue gas from fossil fuel-fired power plants using dry regenerable alkali metal-based sorbent, Progress in Energy and Combustion Science , 2013, 39, 515-534.

[22] H. Gupta , L.−S. Fan, Carbonation-Calcination cycle using high reactivity calcium oxide for carbon dioxide separation from flue gas, Journal of Industrial and Engineering Chemistry , 2002, 41, 4035-4042

[23] H. Chen, C. Zhao, W. Yu, Calcium-based sorbent doped with attapulgite for $CO_2$ capture, Applied Energy,2013, 112, 67-74.

[24] R. Sun, Y. Li, H. Liu, S. Wu, C. Lu, $CO_2$ capture performance of calcium-based sorbent doped with manganese salts during calcium looping cycle, Applied Energy, 2012, 89, 368-373.

[25] V. Manovic, EJ. Athony, Thermal activation of CaO-based sorbent and self-reactivation during $CO_2$ capture looping cycles, Environmental Science & Technology, 2008, 42, 4170–4174.

[26] Y. Li, C. Zhao, L. Duan, C. Liang, Q. Li, W. Zhou, H. Chen, Cyclic calcinations/carbonation looping of dolomite modified with acetic acid for $CO_2$ capture, Fuel Process Technology, 2008, 89, 1461–1469.

[27] Y. Li, C. Zhao, H. Chen, L. Duan, X. Chen, Cyclic $CO_2$ capture behavior of $KMnO_4$-doped CaO-based sorbent, Fuel, 2010, 89(3), 642–649.

[28] N. Shigemoto, T. Yanagihara, Material balance and energy consumption for $CO_2$ recovery from moist flue gas employing $K_2CO_3$-on-Activated Carbon and Its evaluation for practical adaptation, Energy&Fuels, 2006, 20, 721-726.

[29] H. Hayashi, J. Taniuchi, N. Furuyashiki, S. Sugiyama, S. Hirano, N. Shigemoto, T. Nohaka, Efficient recovery of carbon dioxide from flue gases of coal-fired power plants by cyclic Fixed-Bed operations over $K_2CO_3$-on-carbon, Industrial & Engineering Chemistry Research,1998, 37, 185-191.

[30] D. A. Green, B. S. Turk, J. W. Portzer, R. P. Gupta, W. J. McMichael, Y. Liang, T. Moore, D. P. Harrison, Carbon Dioxide Capture from Flue Gas Using Dry Regenerable Sorbents: Quarterly Technical Progress Report; Research Triangle Institute: Research Triangle Park, NC, October, 2001.

[31] C. Zhao, X. Chen, C. Zhao, Carbonation and Active-component-distribution behaviors of several potassium-based sorbents, Industrial & Engineering Chemistry Research, 2011,50, 4464-4470.

[32] D. A. Green, B. S.T urk, J. W. Portzer, R. P. Gupta, W. J. McMichael, T. Nelson et al., Carbon dioxide capture from flue gas using dry regenerable sorbents, Topical Report (2000.9-2004.9), Research Triangle Institute, 2004.

[33] C. Zhao, Y. Guo, C. Li, S. Lu, Removal of low concentration $CO_2$ at ambient temperature using several potassium-based sorbents, Applied Energy, 2014, 124,

241-247.

[34] M. Sevilla, A. B. Fuertes, Sustainable porous carbons with a superior performance for $CO_2$ capture, Energy & Environmental Science, 2011, 4, 1765-1771.

[35] C. Zhao, X. Chen, C. Zhao, $CO_2$ absorption using dry potassium-based sorbents with different supports, Energy Fuels, 2009, 23, 4583-4687.

[36] A. G. Okunev, V. E. Sharonov, Y. I. Aristov, V. N. Parmon, Sorption of carbon dioxide from wet gased by $K_2CO_3$-in-porous matrix: influence of the matrix nature. Reaction Kinetics and Catalysis Letters, 2000, 71(2), 355-362.

[37] G. Xiao, R. Singh, A. Chaffee, P. Webley, Advanced adsrobents based on MgO and $K_2CO_3$ for capture of $CO_2$ at elevated temperatures, International Journal of Greenhouse Gas control, 2011, 5, 634-639.

[38] S. Hirano, N. Shigemoto, S. Yamada, H. Hayashi, Cyclic fixed-bed operation over $K_2CO_3$-on-carbon for the recovery of carbon dioxide under moist conditions, Bulletin of the Chemical Society of Japan, 1995, 68, 1030-1035.

[39] R. W. Pekala, Organic aerogels from the polycondensation of resorcinol with formaldehyde, Journal of materials Science, 1989, 24, 3221-3227.

[40] C. Robertson, R. Mokaya, Microporous activated carbon aerogels via a simple subcritical drying route for $CO_2$ capture and hydrogen storage, Microporous and Mesoporous Materials, 2013, 179, 151-156.

[41] D. Faire'n-Jime'nez, F. Carrasco-Mari'n, C. Moreno-Castilla, Porosity and surface area of monolithic carbon aerogels prepared using alkaline carbonates and organic acids as polymerization catalysts, carbon, 2006, 44, 2301-2307.

[42] S. A. Al−Muhtaseb, J. A. Ritter, Preparation and Properties of Resorcinol-Formaldehyde Organic and Carbon Gels, Advanced Materials, 2003, 15(2),

101-114.

[43] E. Bahn, O. Czakkel, B. Nagy, K. László, S. V-Rodil, J. M. D. Tascón, F. Demmel, M. T. F. Telling, P, Fouqent, Diffusion of molecular hydrogen in carbon aerogel, Carbon, 2016, 98, 572-581.

[44] O. Czakkel, K. Marthi, E. Geissler, K. László, Influence of drying on the morphology of resorcinol-formaldehyde-based carbon gels, Microporous and Mesoporous Materials, 2005, 86, 124-133.

[45] H. Tamon, H. Ishizaka, T. Yamamoto, T. Suzuki, Preparation of mesoporous carbon by freeze drying, Carbon, 1999, 37, 2049-2055.

[46] O. Czakkel, E. Székely, B. Koczka, E. Geissler, K. László, Drying of resorcinol-formaldehyde gels with $CO_2$ medium, Microporous and Mesoporous Materials, 2012, 148, 34-42.

[47] S. J. Taylor, M. D. Haw, J. Sefcik, and A. J. Fletcher, Gelation mechanism of resorcinol-formaldehyde gels investigated by dynamic light scattering, Langmuir, 2014, 30, 10231-10240.

[48] C. Lin, J. A. Ritter, Effect of synthesis PH on the structure of carbon xerogels, Carbon, 1997, 35(9), 1271-1278.

# Chapter 2: The basic theory

## 2.1 Adsorption and desorption

Sorption consists of adsorption and absorption. Adsorption is the adhesion of ions, atoms, or molecules from a gas, liquid, or dissolved solid to a surface which is a boundary between two phases such as solid-liquid, solid-gas, and liquid-gas phases. Absorption is an adsorbate permeates or dissolved by a liquid or solid. The distinction between adsorption and absorption would vanish when absorbents are porous materials, aggregates and composites made out of nanoparticles. The international union of pure and applied chemistry (IUPAC) term divided adsorption into physical adsorption which is induced by weak van der Waals force (~10–100 meV), and chemical adsorption which has been given rise to a formation of chemical compounds with stronger interaction energy than physical adsorption [1].

## 2.2 Porosity

The pore structure of a material determined the physical properties such as density, thermal conductivity and strength, and tailored the nanoporous structure play an important role in industrial applications in design of catalysts, industrial adsorbents and so on [16]. Just as showed in Figure2-1 IUPAC classified pores according to the availability to an external fluid.

**Closed pores**: totally isolated to other pores, as the region (a) showed in Figure 2-1, these types of pores may influence density, mechanical strength and thermal conductivity of porous material.

**Open pores**: possess a continuous channel and communicate with the external surface. Open pores are further categorized into blind pores like (b) and (f), through pores like type (e). These pores contribute to the physical adsorption and sequestration of gases, hydrogen storage and other industrial field.
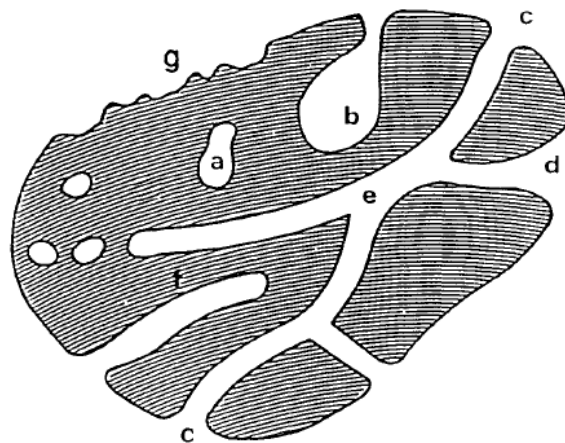


**Figure 2-1:** Schematic cross-section of a porous solid [16]

Porosity is a fraction of the volume of voids to the total volume. Properties of material are important in practical applications such as pore size, pore value, and specific surface area. Just as chapter1 discussed that the nature of porosities play an important role in capturing $CO_2$ when load Alkali-metal carbonate onto the porous materials. Pore size classification will be different ascribe to geometry reaction of various pore sizes in a different way under same condition. In the paper of Zdravkov et al. [17], they summarized the various categories of pore sizes into four groups. According to the International Union of Pure and Applied Chemistry (IUPAC) recommendation, Table 2-1 showed the pore sizes are classified as micropore (< 2 nm), mesopore (2−50 nm) and macropore (> 50 nm). Micropore had been divided into ultramicropore (<0.7 nm) and supermicropore (0.7-2 nm) [2].

**Table 2-1:** The classification of pores

| Term | | Pore size (nm) |
|---|---|---|
| Micropore | Ultramicropore | $w < 0.7$ |
| | Supermicropore | $0.7 < w < 2$ |
| Mesopore | | $2 < w < 50$ |
| Macropore | | $w > 50$ |

## 2.3 The adsorption isotherm

A solid material is exposed in a closed space to a gas at definite pressure lead to adsorb the gas and accompany by an increase in the weight of the solid and a decrease in the pressure of the gas [3]. The amount of gas adsorption could be calculated when the pressure and weight increase become cease from volumetric mothed or gravimetric mothed by the increase in weight. The adsorption of a gas by a solid can receive valuable information such as pore structure and specific surface area, and nitrogen adsorption at 77 K (boiling point) is the most commonly used for investigating the porosity. As Figure2-2 shows that adsorption isotherms could be grouped into six types by IUPAC. The brief description of the isotherms will be introduced as follows [18]:
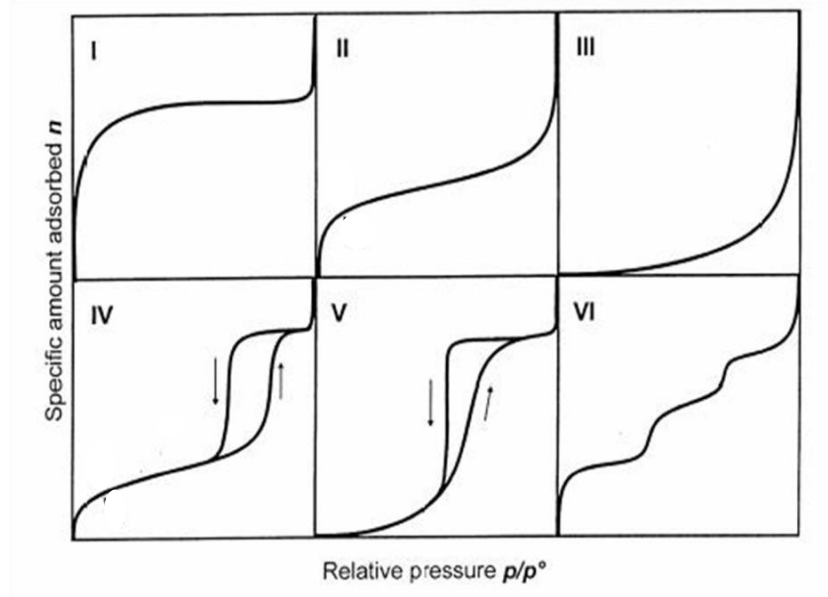
**Figure 2-2:** The IUPAC classification for adsorption isotherms [3, 4].

**Type I isotherms**

Type I isotherms which also has been called Langmuir isotherm are characterized by a plateau which is nearly horizontal and may show a cut or tail in the relative pressure close to 1, representing the adsorption of microporous solid. Because the pore size is not very much greater than the molecular diameter of the sorbate molecule, the potential fields will overlap and interaction energy between the solid and gas molecule will be enhanced cause a complete filling of the pores at a low relative pressure. Many Type I isotherms exhibit no hysteresis at all which can be yield from titania, alumina and so on.

**Type II isotherms**

Type II isotherms well known as BET-type isotherms [5] are typically obtained in case of monolayer-multilayer adsorption on a non-porous or macroporous adsorbent. The curve where emerges a suddenly steep indicates the completion adsorption of the first layer, with the increase of relative pressure, the multilayer has been completed.

**Type Ⅲ isotherm**

Type III isotherm is characteristic of weak gas-solid interactions, could be yield from a nonporous or macroporous solid. The weakness of the solid-gas forces will lead to a small uptake at the low relative pressures, but once a molecule has been adsorbed, the interaction force will be promoted, result in a further adsorption. So the isotherms will become convex to the pressure and persists throughout their course.

**Type Ⅳ isotherm**

Type Ⅳ isotherms are typical for mesoporous solids. There is a flat in the high relative pressure, indicating the completion of mesopores adsorption. Near the $P/P_0=1$ appear a steep because of the adsorption of macropores. Different from other isotherms Type Ⅳ isotherms have an adsorption hysteresis which could not be reversible associate with capillary condensation taking place in mesopores. Usually desorption isotherm is above to the adsorption isotherm.

**Type Ⅴ isotherm**

Type Ⅴ isotherms indicate adsorption by a mesoporous or microporous solid and possess the convexity towards to relative pressure axis. In comparison with Type III isotherm, Type Ⅴ isotherm has a point of inflection at high relative pressure, so the isotherm bends over and reaches a plateau in the multilayer region.

**TypeⅥ isotherm**

Type Ⅵ isotherm, this kind of isotherms is obtained from stepwise multilayer adsorption is called step-wise isotherm, typically obtained from nonporous adsorbates which possesses a nonpolar and uniform surface. For instance, graphitized carbon black which possesses a high uniform surface absorbs krypton at 90K.

## 2.4 Theories of adsorption

2.4.1 The Langmuir theory [6]

The simplest theoretical model for monolayer adsorption is Langmuir equation which was originally developed to represent chemisorption on distinct localized adsorption sites. This theory also has some disadvantages such as parameters vary from site to site (temperature, pressure), ignores the interactions between adsorbate and adsorbate. There are four basic assumptions when use Langmuir theory:

1) Molecules are adsorbed at a fixed number of well-defined localized sites.

2) Each site can hold one adsorbate molecule.

3) All sites are energetically equivalent.

4) There is no interaction between molecules adsorbed on neighboring sites.

2.4.1.1 Kinetic derivation

The velocity ($\mu$) of adsorption can be presented by absolute temperature (T), pressure of gas ($P$), molecular weight of adsorbed gas (M), and gas constant (R).

$$\mu = \frac{P}{(2\pi MRT)^{1/2}} \tag{2-1}$$

The sum between the vacant surface sites ($\theta_0$), and occupied surface sites ($\theta$) is 1. If there is a partial ($a$) conflict to the surface of adsorbent, so $a$ will be in proportion to the $\alpha\mu$ and vacant surface sites ($\theta_0$), and the adsorption velocity of $a$ can be presented by the equation (2-2), and desorption velocity ($\upsilon_d$) has been derived by adsorption process and showed in formula (2-3),

$$v_a = k_a \theta_0 \mu \tag{2-2}$$

$$v_d = k_d \theta \tag{2-3}$$

When the adsorption process achieve to the equilibrium, adsorption velocity is equal to the desorption velocity and from $\theta_0+\theta=1$, we can get (2-4),

$$\theta = \frac{k_a a \mu}{(k_d + k_a a \mu)} \tag{2-4}$$

According to the basic assumptions, if the number of site is $N_0$, and the number of occupied surface site is N, we can get $\theta = N/N_0$, and use A replace N, a substitute $k_a a/k_d \, (2\pi MRT)^{1/2}$, and definite $N_0 = b$. Langmuir formula can be represented by follow.

$$A = \frac{abp}{(1+aP)} \tag{2-5}$$

2.4.2 The Brunauer, Emmett, and Teller (BET) Adsorption Theory [4, 7]



i = 8
i = 7
i = 6
i = 5
i = 4
i = 3
i = 2
i = 1
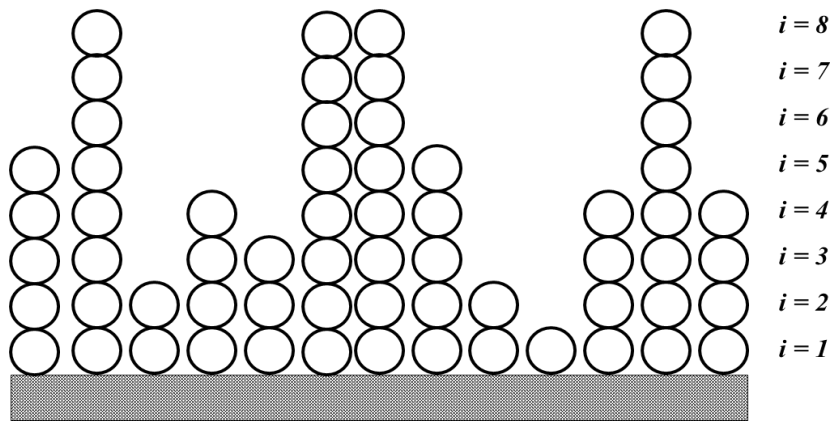
**Figure2-3:** The model of BET multilayer adsorption

Brunauer, Emmett, and Teller developed a simple model isotherm to account for multilayer adsorption and used this model to extract the monolayer capacity and specific surface area (SSA) which is a scientific value that can be used to determine the type and

properties of a material. BET theory has three hypotheses: 1) gas molecules physically adsorb on a solid in layer infinitely; 2) there is no interaction between each adsorption layer; and 3) the Langmuir theory can be applied to each layer. Figure 2-2 presents the BET multilayer model, where $i$ is the number of layers, and $s_i$ is the sites formed $i$-numbers molecular layers.

For the first layer adsorption which is expansion from Langmuir equation just as described above. When the adsorption system at an equilibrium status, the relationship can be presented by:

$$a_1 P s_0 = b_1 s_1 \exp(- Q_1/RT) \tag{2-6}$$

Where $Q_1$ is the molecular adsorption energy of first layer, $a_1$ and $b_1$ are the constant, and $p$ is pressure of gas. There is an assumption that the adsorption energy not depend on the number of adsorbed molecules and then the BET theory assumes that there has an energy equivalent on every layers.

Similarly, for $i$-layers at equilibrium status, the formula can be changed to:

$$a_i P s_{i-1} = b_i s_i \exp(- Q_i/RT) \tag{2-7}$$

$s_0$ is the adsorption capacity of all the adsorbed molecules ($v$) is presented by $v = \sum_{i=0}^{\infty} i s_i$, and then, the monolayer adsorption capacity can be derived as $v_m = \sum_{i=0}^{\infty} s_i$. Because the hypothesis that the adsorption energy above second layers is equivalent to liquid cohesive energy ($Q_L$), so the equation can be given:

$$Q_2 = Q_3 = \cdots\cdots Q_i = Q_L \tag{2-8}$$

Above the second layers, the interaction between molecules adsorbed is significantly

smaller than the interaction between the first layer and the solid surface. So the ratio of $a_i$, $b_i$ is also regarded as constant (g).

$$b_2/a_2 = b_3/a_3 = \cdots\cdots = b_i/a_i = g \tag{2-9}$$

Additionally, x and c are replace by

$$(p/g)\exp(Q_L/RT) = x \tag{2-10}$$

$$(a_1g/b_1)\exp[(Q_1 - Q_L)/RT] = C \tag{2-11}$$

Because,

$$v/v_m = \sum_{i=0}^{\infty} is_i / \sum_{i=0}^{\infty} s_i \tag{2-12}$$

We can get the equation

$$\frac{v}{v_m} = \frac{Cx}{(1-x)(1-x+Cx)} \tag{2-13}$$

Substitute x=1, p=$p_0$ into equation (2-10), then compare with it, we can know x indicates a relative pressure.

$$x = P/P_0 \tag{2-14}$$

By formula (2-14), (2-13) could be rewritten as formula (2-15), this equation is called BET adsorption isotherm.

$$v = \frac{v_m CP}{(P_0-P)\left(1+(C-1)(P/P_0)\right)} \tag{2-15}$$

The BET equation can be written as

$$\frac{P}{v(P_0-P)} = \frac{1}{v_mC} + \frac{C-1}{v_mC} \times \frac{P}{P_0} \tag{2-16}$$

Figure 2-4 shows the relationship between the relative pressure and $P/v(P_0-P)$, plotting

along abscissa and ordinate respectively. The value of intercept and slope of the line are used to calculate the monolayer adsorption capacity ($v_m$) and the BET constant C. Generally, the linear relationship of this equation is maintained in the range of p/p$_0$ from 0.05 to 0.35, where the coverage rate ($\theta=v/v_m$) is from 0.5 to 1.5. Specific surface area (A$_S$) can be determined by BET theory through the following equation:

$$A_s = (v_m N a_m / M) \times 10^{-18} \qquad [m^2/g] \qquad (2\text{-}17)$$

Where $N$ is Avogadro constant ($6.022 \times 10^{-23}$), $a_m$ is molecular cross-section area and $M$ presents the molecular weight of adsorbed molecule.
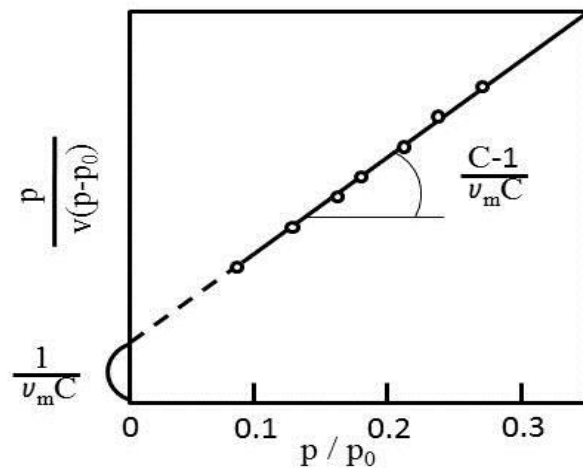


**Figure2-4:** BET plot [the relationship between $P/v(P_0\text{-}P)$ and $P/P_0$ ]

### 2.4.3 α$_s$-Plot method

α$_s$ −Plot was recommended by K. S. W. Sing [8] which is similar to t-plot and is not restricted to nitrogen. This method do not need consider the numerical thickness since the object is merely to compare the shape of the isotherm with the standard adsorption

isotherm, it is not necessary to involve the number of molecular layers or the monolayer capacity, and it is available for other adsorbate besides nitrogen. Sing defined the $\alpha_S$ value as the relative adsorption amount of a standard sample, so $\alpha_s = A/A_{0.4}$, where A present the adsorption capacity of the sample, and $A_{0.4}$ is the adsorption amount at relative pressure $P/P_0 = 0.4$. If a straight line through the origin results, one may infer that the isotherm is identical in shape with the standard, and the slope of the isotherm is equivalent to $V_{0.4}$.

To estimate the specific surface area ($A_s$) of a test sample, we can use the follow equation which is calculated from the slope ($S$) of the $\alpha_S$-plot:

$$A_s = [S(sample)/S(standard)] \times A(standard)A_s \qquad (2\text{-}18)$$

## 2.5 Characterization methods

2.5.1 Thermogravimetric-differential thermal analysis (TG-DTA)

Thermogravimetric analysis (TGA) is an essential laboratory tool used for material characterization in which changes in physical and chemical properties of materials are measured as a function of increasing temperature, or as a function of time. TGA can provide information about physical phenomena and chemical phenomena [9], which is applicable to most industries, such as environmental, food science, pharmaceutical, and petrochemical through the Thermogravimetric analysis [10].

TGA is commonly used to determine selected characteristics of materials that exhibit either mass loss or gain due to decomposition, oxidation, or loss of volatiles. Common applications of TGA are (1) materials characterization through analysis of characteristic decomposition patterns, (2) studies of degradation mechanisms and reaction kinetics,

(3) determination of organic content in a sample, and (4) determination of inorganic content in a sample.

TGA instruments can be divided into two general types: vertical and horizontal balance. Vertical balance instruments have a specimen pan hanging from the balance, it is important to calibrate these instruments in order to compensate for buoyancy effects stem from the variation in the density of the purge gas which is change with temperature, as well as the type of gas. However, horizontal balance instruments normally have two pans (sample and reference), which are considered free from buoyancy effects [11]. In this research, the thermal stability of CAs, decomposition temperature of composites, and $CO_2$ capture capacity had been measured by TG-DTA method.

2.5.2 X-Ray Diffraction (XRD)

X-Ray Diffraction is a tool used for identifying the atomic and molecular structure of a crystal, in which the crystalline atoms cause a beam of incident X-rays to diffract into many specific directions. By measuring the angles and intensities, which could measure the average spacings between layers or rows of atoms, determine the orientation of a single crystal or grain, find the crystal structure of an unknown material, measure the size, shape and internal stress of small crystalline regions and discern materials that appear similar by other experiments [12].

English physicists Sir W. H. Bragg and his son Sir W. L. Bragg developed a relationship in 1913 to explain why the cleavage faces of crystals appear to reflect X-ray beams at certain angles of incidence [13]. X-ray diffraction can be explained by the Bragg's Law: $n\lambda = 2d\sin\theta$, in this equation d represent the distance between atomic layers in a crystal, $\lambda$ delegate the wavelength of the incident X-ray beam, $\theta$ is angle of

incidence of reflect X-ray beam and  n is an integer. Figure 2-5 shows the details of Bragg's Law. In this dissertation, the structure of carbonation and decarbonation of composites before and after $CO_2$ adsorption had been measured by X-Ray diffraction.
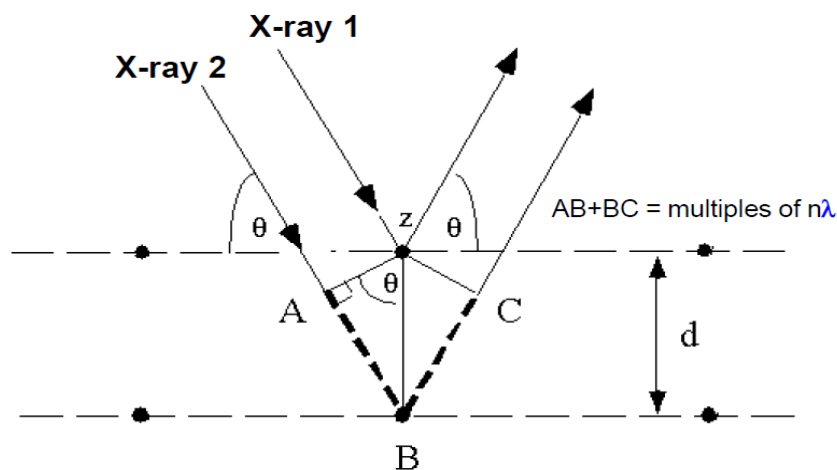


**Figure 2-5:** X-Ray Diffraction-Bragg's Law [13]

$K_2CO_3$ will convert to $K_2CO_3.1.5H_2O$ in few minutes in the atmosphere result from the deliquescent property that $K_2CO_3$ would capture water quickly in the air. After we used TG-DTA device to decompose the composites who were loaded with $K_2CO_3$, it is difficulty to forbid composites contact with water in the air because we have to bring the sample from three floors to eight floors, and the process of setting the sample into the glass plate also increase the chance of contacting with air. Even though the vacuum XRD will evacuate water from composites, it is still cannot be removed completely. So in order to avoid this affect the experimental data, just as Figure 2-6 showed we putted the ribbon heater into the cavity which is exactly below the measured samples, and increase the temperature to 453 K gradually, the heating rate cannot be controlled and remain stability, it is dangerous to increase the heater to destination temperature, we should pay attention to the interval increment, such as 50 degree gradual rise. When the

heater reached the set point, the temperature was maintained for 2 hours for pretreatment.
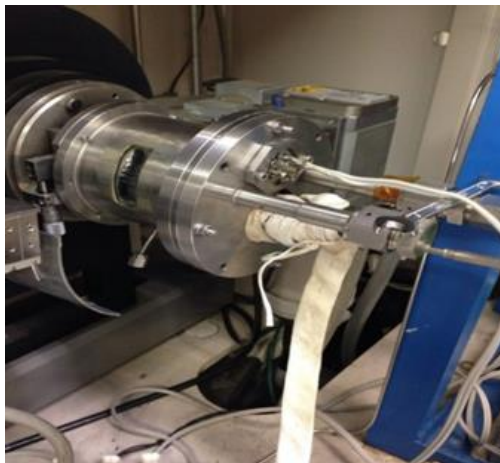


**Figure 2-6:** In-situ X-Ray diffraction

2.5.3 Water adsorption

The isolated water molecule has an O-H bond length of 0.9575 Å, with the two H atoms and the lone pairs arranged approximately tetrahedrally around the central oxygen, with an HOH bond angel of 104.5 degree [14]. Water adsorption by porous materials play an important role in many application that require absorb and release of water, such as dehumidification, gas storage and separation, and thermal batteries [15]. The adsorption capacity of water has a closed connection with the properties of porous materials which possess a hydrophilic surface or a hydrophobic surface. Water adsorption model has been intensively studied by many researches, McCallum et al. investigated water adsorption model on activated carbon from simulation and experiment, provided two simplification models which showed in Figure 2-7, A is regular sites allocation and B corresponds to a random array of sites. The process was

classified into 5 steps, water molecules adsorbed onto surface sites, all sites were occupied, and then water-water adsorption by H-bonding, the formation of water cluster, in the last stage pore would be filled by water molecules. They also used 4 kinds of pore sizes to adsorb water in simulation, and found that the smaller pore size display greater adsorption at low pressure, and pore filling also occur at a low relative pressure [19]. A cluster growth mechanism was elucidated by Kaneko et al. when the hydrophobic nanopores were free of surface functional groups, water vapor rarely be absorbed below $P/P_0=0.5$, when relative pressure exceeded to 0.6, isolated water molecules would associate with each other to form clusters and the give rise to an extraordinary aggregation of these water cluster. There are two reason can affect the existence of hysteresis and the hysteresis shape between the adsorption and desorption isotherm of water, which are pore size of micropores (width of pore above 0.7 nm will produce remarkable hysteresis), and surface functional groups could influence the hysteresis shape because of the various interaction capacity with water [20, 21].
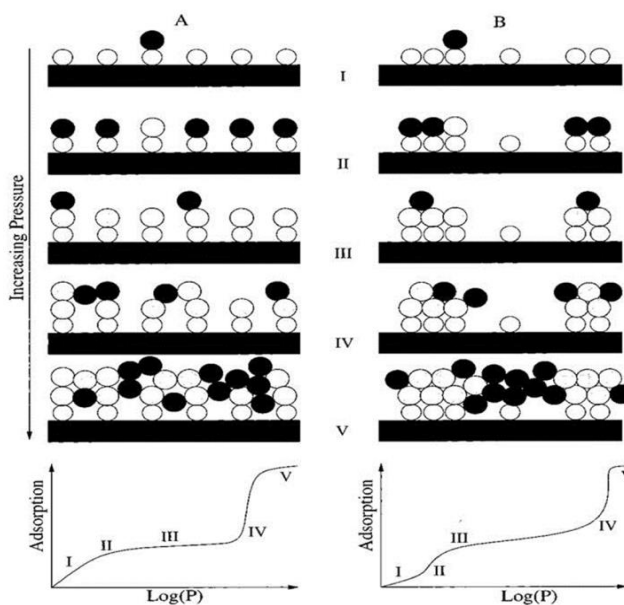


**Figure 2-7:** Two possible mechanisms for water adsorption onto activated carbon walls

[19].

In $CO_2$ capture process, just as mentioned in the previous chapter, water adsorption is often detrimental for $CO_2$ capture. If we want to invest a prominent material which is stable to water, and the porous structure will not be changed by capturing and releasing $H_2O$, it is important to investigate the water sensitivity to adsorbents because water adsorption acts as a strong competitor when using hydrophilic material in $CO_2$ capture process. And in this research, we used the device which is showed in Figure 2-8 to measure the water adsorption capacity of CAs, composites, and $K_2CO_3$, according increase or decrease the pressure of water, measuring the mass change of samples in the glass basket. We putted samples in (2), and recorded the scale position before and after pretreatment that vacuum the device by the order from open (4) and the rotary knob of (3) and (2) little by little to avoid the blow off of samples. After the vacuum indicator did not change anymore, we would operate diffusion vacuum by closing (4), opening the (5) and (6), maintain this process for 2 hours and then close the diffusion vacuum by the reverse order. Liquid nitrogen was installed in (3), precipitating water in the vacuum process and avoid water entering into pump (7). (8) is contact with atmosphere, after measurement we open (8) gradually to make the water line change to the same pressure with atmosphere.
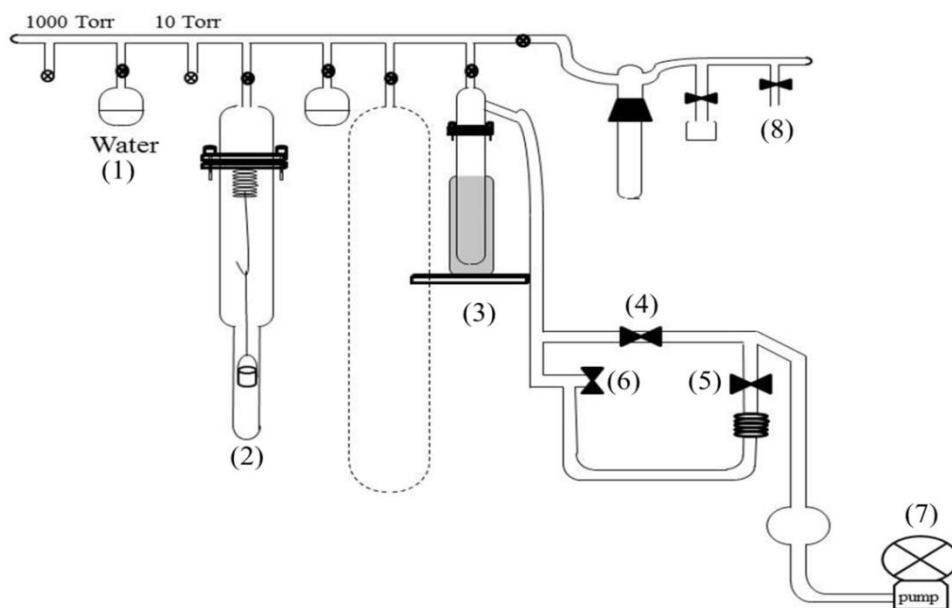
**Figure 2-8:** the equipment of water adsorption

2.5.4 Multi-step CaO solution for $CO_2$ precipitation

In $CO_2$ capture process, it is complicated to measure the $CO_2$ uptake from composites, sometimes it will be overestimated the capacity of $CO_2$ capture by using TG-DTA experiment, because porous materials may prefer adsorb $H_2O$ to $CO_2$. So we used CaO solution to verify the amount of $CO_2$ adsorption. Calcium oxide (CaO), commonly known as quicklime or burnt lime, is a widely used chemical compound. It is a white, caustic, alkaline, crystalline solid at room temperature. CaO is difficult dissolve in water, and lower temperature of water, the higher solubility. The reactions have been showed as (2-19) and (2-20) equations:

$$CaO \ (s) + H_2O \ (l) \ \rightarrow \ Ca(OH)_2 \ (l) \tag{2-19}$$
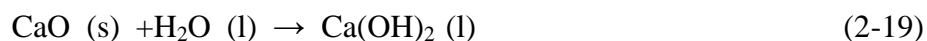
Firstly, prepare the saturated Calcium hydroxide solution by adding excess Calcium oxide into water, and filtering the white precipitation contribute to the dissolved residual CaO.

$$Ca\,(OH)_2\,(l)+CO_2\,(g) \rightarrow CaCO_3\,(s)+H_2O\,(l) \qquad\qquad (2\text{-}20)$$
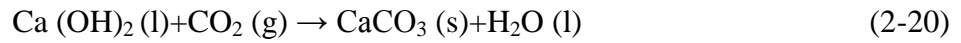
Calcium hydroxide solution had been used to capture $CO_2$ which is released from composites after carbonation by TG-DTA experiment. And then weigh the precipitation elaborately. We designed the device of this process, which is showed in Figure 2-9, by using multi-step for completely adsorption.
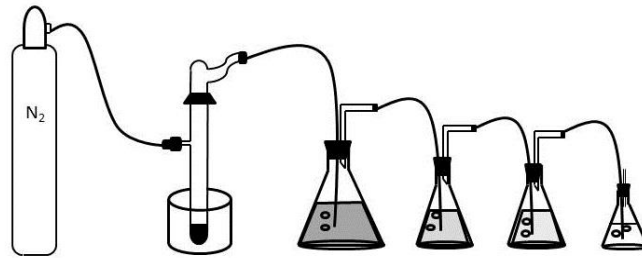


**Figure 2-9:** The device of multi-steps Cao solution for $CO_2$ precipitation

# References

[1] IUPAC manual of symbols and terminology for physicochemical quantities and units. Pure and Applied Chemistry,1972, 31(4), 577-638

[2] F. Rouquerol, J. Rouquerol, K. Sing, Adsorption by Powders and Porous Solid, Academic press, London, 1999.

[3] S. J. Gregg, K. S. W. Sing,  Adsorption, Surface Area and Porosity. 1991

[4] K. S. W. Sing, D. H. Everett, R. A. W. Haul, L. Moscou, R. A. Pierotti, J. Roquerol, T. Siemieniewska, Pure and Applied Chemistry, 1985, 57, 603-619

[5] S. Brunauer, P. H. Emmett, E. Teller, Adsorption of gases in multimolecular layers, Journal of The American Chemical society, 1938, 60, 309−319

[6] D. M. Ruthven, Principles of adsorption and adsorption processes, University of New Brunswich, Fredericton

[7] K. S. W. Sing, Reporting physisorption data for gas/solid systems with special reference to the determination of surface area and porosity, Pure and Applied Chemistry, 54(11), 2201-2218

[8] K. S. W. Sing, Proceedings of the conference on porosity and carbon materials: measurements and applications, Carbon, 1989, 27(1), 1-170

[9] https://en.wikipedia.org/wiki/Thermogravimetric_analysis

[10]http://www.perkinelmer.com/cmsresources/images/4474556gde_tgabeginnersguide.pdf

[11]http://www.uzaktanegitimplatformu.com/UEP/uep_ylisans/ey2/ey2_download/Practice%20Guide_Section%202_TGA.pdf

[12] https://en.wikipedia.org/wiki/X-ray_crystallography

[13]http://www.google.com.hk/url?sa=t&rct=j&q=&esrc=s&source=web&cd=1&ved=0

CB8QFjAAahUKEwiuveeOut_IAhXMF5QKHcyxABw&url=http%3A%2F%2Fweb.pd

x.edu%2F~pmoeck%2Fphy381%2FTopic5a-XRD.pdf&usg=AFQjCNGy7zZnnBpLrlIP

Vbji6_YcLQSlpg

[14] A. Hodgson, S. Haq, Water adsorption and the wetting of metal surfaces, Surface Science Reports, 2009, 64, 381-451

[15] H. Furukawa, F. Gandara, Y−B. Zhang, J. Jiang, W. L. Queen, M. R. Hudson, O.M. Yaghi, Water adsorption in porous metal-organic frameworks and related materials, Journal of The American Chemical society, 2014, 136, 4369-4381

[16] Recommendations for the characterization of porous solids, Pure and Applied Chemistry, 1994, 66(8), 1739-1758.

[17] B. D. Zdravkov, J. J. Čermák, M. Šefara, J. Janků, Pore classification in the characterization of porous materials: A perspective, Central European Journal of Chemistry, 2007, 5(2), 385-395.

[18] K. Kaneko, Determination of pore size and pore size distribution 1. Adsorbents and catalysts, Journal of Membrane Science, 1994, 96, 59-89.

[19] C. L. McCallum, T. J. Bandosz, S. C. McGrother, E. A. Müller, and K. E. Gubbins, A molecular model for adsorption of water on activated carbon: comparison of simulation and experiment, Laugmuir, 1999, 15, 533-544.

[20] K.Kaneko, Y. Hanzawa, T. Iiyama, T. Kanda, and T. Suzuki, Cluster-mediated water adsorption on carbon nanopores, Adsorption, 1999, 5, 7-13.

[21] T. Ohba, H. Kanoh, and K.Kaneko, Water cluster growth in hydrophobic solid nanospaces, Chemistry-A European Journal, 2005, 11, 4890-4894.

# Chapter 3: $CO_2$ capture by carbon aerogel–potassium carbonate nanocomposites

## 3.1 Introduction

Carbon dioxide ($CO_2$) is the principal greenhouse gas. It has been continuously released into the environment through the burning of fossil fuels and has led to global warming and anthropogenic climate change, such as droughts, desertification, permafrost melt, inundation, rising sea levels, and ecosystem disruption, and it is expected to substantially affect the future of mankind. Although alternative energy sources have been extensively investigated, no single alternative source can satisfy global energy demands; fossil fuels are therefore expected to remain the primary energy resource for the next several decades because of their advantages of low cost and high energy density. The atmospheric $CO_2$ concentration was 384 ppm in 2007 and is expected to reach 550 ppm by 2050; hence, mitigating the atmospheric $CO_2$ concentration is critical for protecting our environment [1, 2]. With both high $CO_2$ capture capacity and low cost, alkali metal carbonates ($M_2CO_3$, M = K, Na) have been recognized as potential sorbents for $CO_2$ sorption according to the following reaction [3]:

$$M_2CO_3 \text{ (s)} + H_2O \text{ (g)} + CO_2 \text{ (g)} \rightleftarrows 2MHCO_3(s). \qquad (3\text{-}1)$$

The forward reaction is a bicarbonate formation reaction (the theoretical $CO_2$ capture capacity is 7.24 mmol-$CO_2$/g-$K_2CO_3$), whereas the reverse reaction is an endothermic regeneration process that begins at 445.3 K and ends at 548.1 K when the heating rate is 20 K/min [4].

In recent years, to solve problems such as the slow reaction rate of bicarbonate formation and high energy consumption during regeneration, researchers have extensively investigated various composites containing alkali metal carbonates [5-8]. The regeneration behaviors of alkali metal carbonates change when they are supported on nanoporous structural materials such as activated carbon, $Al_2O_3$, or carbon nanofibers or when they are combined with MgO, TiO, or FeOOH, which can themselves capture $CO_2$. Because of the antagonistic relationship between the effects of high regeneration temperatures and low capture capacities, suitable materials have not been developed. Zhao et al. reported that $K_2CO_3$ sorbents exhibit better $CO_2$ capture performance than $Na_2CO_3$ sorbents and that the selection of a support material with appropriate characteristics is important for carbonation and regeneration [9]. We also previously reported a detailed reaction mechanism for $CO_2$ occlusion by $K_2CO_3$ under moist conditions [10, 11]. Therefore, in the present study, we focus on impregnating $K_2CO_3$ into the nanopores of carbon aerogels (CAs) prepared by pyrolysis of a dried organic aerogel followed by carbonation, leading to the formation of vitreous black monoliths with highly cross-linked micropores and mesopores [12, 13]. The CAs provide a suitable mesoporous reaction field for forming $K_2CO_3$ nanocrystals because the CAs' surface area, pore structure, and size are easily controlled through manipulation of the molar ratios among reagents or the pH [14, 15]. In the present paper, the $CO_2$ capture ability of $K_2CO_3$ nanocrystals incorporated into mesopores of CAs is studied from the viewpoint of lowering the regeneration temperature while achieving high selectivity and high capture capacity.

## 3.2 Experimental Section

3.2.1. Preparation of CA

All reagents were purchased from Wako Pure Chemical Industries, Ltd. Resorcinol–formaldehyde (RF) solutions were synthesized under the following experimental conditions. The resorcinol-to-sodium carbonate (R/C) and resorcinol-to-formaldehyde (R/F) molar ratios were fixed at 500 and 0.5, respectively, and the molar ratio of resorcinol to deionized water (R/W) was varied among 0.14, 0.28, and 0.7 to produce RF gels with different pore sizes. For a given R/W ratio, the required resorcinol was weighed out and added to deionized water; the resulting mixture was then stirred until the resorcinol was completely dissolved. Formaldehyde and sodium carbonate were added to the mixture, resulting in yellowish homogeneous RF solutions that were subsequently sealed and placed in a thermostated bath at 303 K for 2 weeks for polymerization [12].

Water entrained within the gel network of the polymer was removed through solvent exchange; the gel was successively soaked in mixed solutions of acetone and water at a ratio of 1:1 and 3:1 and in pure acetone for 15 min each. Finally, the gel was immersed in acetone for 1 day at room temperature. To preserve the structure of the nanoporous material, the wet gel was dried using a supercritical drying process. The wet gel was then placed in a supercritical drying chamber, and $CO_2$ was slowly introduced to bleed the air from the chamber. $CO_2$ was introduced to a pressure of 10 MPa at 318 K and was maintained at this temperature for 3 h. Carbonization of the organic aerogels was conducted at 1173 K for 3 h under Ar flowing at 100 $cm^3$/min. As described later, the porosities of the three different CAs were characterized by $N_2$ gas adsorption measurements at 77 K; the three CAs were observed to have pore widths of 7, 16, and 18 nm; these CAs are denoted as 7CA, 16CA, and 18CA, respectively.

### 3.2.2. Preparation of CA–potassium carbonate (KC) nanocomposites

CA–KC nanocomposites were prepared by impregnating the nanopores of the CAs with a 0.15 mol/dm$^3$ $K_2CO_3$ (99.5% chemical purity) aqueous solution [3]. The mixture was then stirred with a magnetic stirrer for 24 h at room temperature. The aqueous solution was dried at 378 K in a vacuum evaporator. The samples were subsequently dried again in a furnace under an Ar ambient atmosphere at 573 K for 2 h. The nanocomposites are denoted as $x$CA–KC, where $x$ represents the pore width of the CAs.

### 3.2.3. Measurements and characterization

The porosities of the CAs and the $x$CA–KC nanocomposites were characterized by $N_2$ adsorption at 77 K using an Autosorb-MP1 (Quantachrome Instruments). $CO_2$ adsorption was measured using a Belsorp-Mini (MicrotracBEL Corp.). The CA and $x$CA–KC nanocomposites were pretreated by heating to 423 K under vacuum for 2 h before the gas adsorption measurements because $K_2CO_3$ is partially converted into $KHCO_3$ under an ambient atmosphere containing $CO_2$ and $H_2O$. Water adsorption isotherms were obtained by a gravimetric method at 303 K; the equilibration time was 2 h.

The Brunauer–Emmett–Teller (BET) method was used to analyze the specific surface areas ($S_{BET}$) on the basis of linear plots over the relative pressure ($P/P_0$) range 0.05–0.35 for the $N_2$ adsorption isotherm data. The total volume ($V_T$) was obtained at a relative pressure of 0.99, and the Dubinin–Radushkevich equation was used to calculate the micropore volume ($V_{mic}$). The mesopore diameters ($D_{mes}$) were estimated by the Barrett-Joyner-Halenda method.

The amount of $K_2CO_3$ impregnated into the mesopores of CA was determined by thermogravimetry–differential thermal analysis (TG–DTA, Shimadzu DTG-60AH),

where the samples were heated to 1073 K. Because the residue consisted of $K_2CO_3$, the impregnated amounts of $K_2CO_3$ were calculated on the basis of the final TG curves to be 18.5, 21.3, and 18.8 wt% for 7CA–KC, 16CA–KC, and 18CA–KC, respectively.

After the $x$CA–KC nanocomposites were heated to 473 K at 10 K/min under an $N_2$ atmosphere and maintained at 473 K for 5 min to ensure complete formation of $K_2CO_3$, the temperature was decreased to 313 K, and $CO_2$ and $H_2O$ were introduced into the sample chamber of the TG–DTA apparatus for 2 h by flowing $CO_2$ through distilled water. The $x$CA–KC nanocomposites reacted with $CO_2$ and $H_2O$ to form $x$CA–$KHCO_3$. The crystal structures before and after the $CO_2$ capture were measured through ex situ X-ray diffraction (XRD) on an X-ray diffractometer (MAC Science, M03XHF) equipped with a Cu $K\alpha$ radiation source (40 kV, 25 mA, $\lambda = 0.15406$ nm). We heated the $x$CA–$KHCO_3$ nanocomposites to 473 K in order to study the regeneration process under the same conditions used in the aforementioned experiments.

We used the CaO solution–precipitation method to accurately determine the amount of $CO_2$ captured by the $x$CA–KC samples. The detail process was demonstrated in the previous chapter. The CaO solution was prepared by dissolving 0.6 g of CaO in 100 cm$^3$ distilled water. Any insoluble precipitate was filtered to yield a saturated solution. The clear solution was bubbled with $N_2$ gas to remove any dissolved $CO_2$ from air. The nanocomposites, which captured $CO_2$ under moist conditions in the TG–DTA chamber at 313 K, were heated at 573 K, and the desorbed $CO_2$ was recaptured by the CaO solution, leading to the immediate formation of a white precipitate. XRD analysis indicated that the precipitate was $CaCO_3$. Before the $x$CA–KC experiments, the reliability of the CaO solution–precipitation method was evaluated using analytical grade $KHCO_3$ powder, which indicated 92% precision with respect to the theoretical

value.

## 3.3 Results and Discussion

3.3.1 BET surface area and pore size distributions (PSDs) of the CAs and xCA–KCs
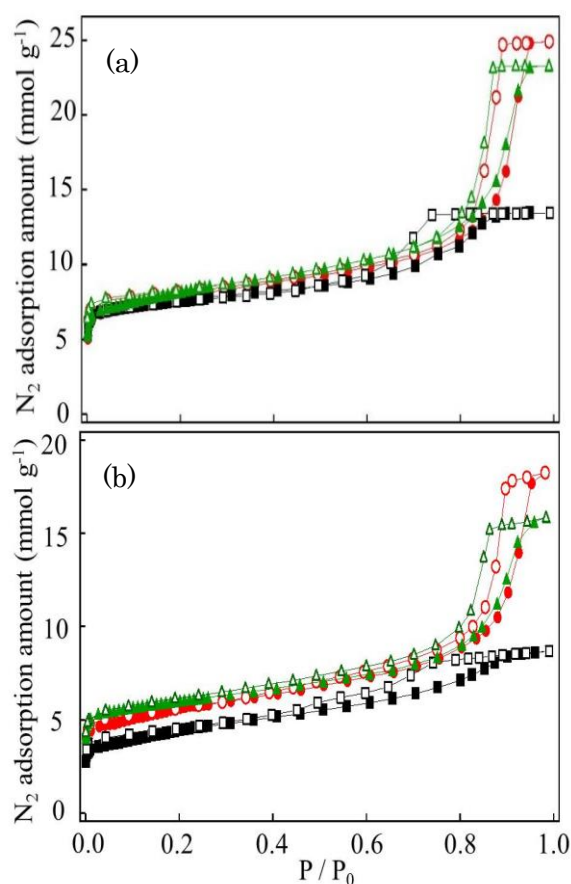


**Figure 3-1:** $N_2$ adsorption isotherms of (a) CAs and xCA–KC samples at 77 K. Pore widths: black, 7 nm; green, 16 nm; red, 18 nm.

The pore structures were characterized using $N_2$ adsorption isotherms volumetrically measured at 77 K after pretreatment at 423 K for 2 h; the obtained isotherms are presented in Figure 3-1. The isotherms of the composites are categorized as type IV (IUPAC classification) with hysteresis between the adsorption and desorption branches which ascribed to the capillary condensation phenomenon. When the relative pressure $(P/P_0)$ was larger than 0.8, the adsorption amount increase sharply, these isotherms

indicate the presence of mesopores, although the increased adsorption at low relative pressures also indicates the presence of micropores. Zhao et al. examined the effects of the pore structure of $Al_2O_3$ supports on the ability of $K_2CO_3$ to capture $CO_2$ and observed that $K_2CO_3$ could quickly convert to $K_2CO_3 \cdot 1.5H_2O$ because of the mesoporous structure of the $Al_2O_3$ support; they also observed that the micropores of the $Al_2O_3$ support facilitated the rapid conversion of $K_2CO_3 \cdot 1.5H_2O$ to $KHCO_3$. Thus, mesoporous structures can enhance $CO_2$ adsorption [8]. In the present study, the $N_2$ adsorption amount decreased for all samples after they were subjected to the $K_2CO_3$ impregnation treatment, indicating that $K_2CO_3$ was successfully incorporated into the micropores and mesopores of the CAs.

The pore structure parameters are compiled in Table 3-1, which shows that the surface area and pore volume of the *x*CA−KC nanocomposites decreased compared with those of the original CAs, this is consistent with the results of $N_2$ adsorption isotherms, which indicate a partial filling or blocking of the pores by impregnated $K_2CO_3$ [6]. The results in Table 3-1 indicate that 16CA possessed the highest surface area and exhibited the greatest decrease in surface area after the $K_2CO_3$ impregnation. This is in agreement with the result that 16CA−KC contained a larger amount of impregnated $K_2CO_3$ compared with other the *x*CA−KCs.

**Table 3-1:** Pore parameters of the xCA and xCA−KC samples

|  | $S_{BET}$ (m$^2$/g) | $V_T$ (cm$^3$/g) | $V_{mic}$ (cm$^3$/g) | $D_{mes}$ (nm) |
|---|---|---|---|---|
| 7CA | 517 | 0.43 | 0.25 | 7.0 |
| 7CA−KC | 357 | 0.30 | 0.14 | 4.0 |
| 16CA | 635 | 0.75 | 0.29 | 16 |
| 16CA−KC | 459 | 0.55 | 0.20 | 12 |
| 18CA | 523 | 0.88 | 0.24 | 18 |
| 18CA−KC | 457 | 0.63 | 0.18 | 14 |

45

3.3.2. Structural changes induced by $CO_2$ capture and regeneration

We loaded $K_2CO_3$ into carbon aerogel, and Figure 3-2 showed the XRD pattern of matrix CA, there are two broadened peaks located at ca. $2\theta$ of $25^o$ and $43^o$ which demonstrated that amorphous carbon was formed and the wide peaks could be recognized as the disorder structure of carbon aerogels. The (002) and (001) reflection correspond to the crystal planes of graphite carbon peak, and Yan et al. reported the property effects to carbon aerogels by using three catalysts which were $Ca(OH)_2$, NaOH, and $Na_2CO_3$, and found $Na_2CO_3$ could produce the largest graphitization extent, that is the (002) peak showed the highest intensity among the three catalysts [26], and highest specific surface area, relatively narrower pore size. After loading composites xCA-KC showed additional peaks which reflect the success of $K_2CO_3$ impregnation. The XRD pattern of carbonation and regeneration phase described as follow.
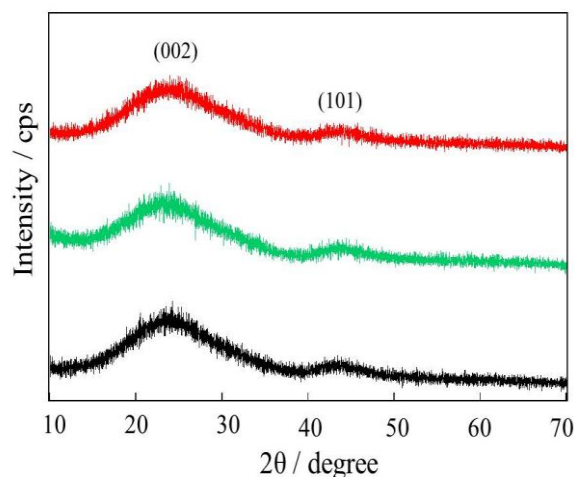


**Figure 3-2:** XRD pattern of carbon aerogel. Pore width: black, 7 nm; green, 16 nm; red, 18 nm

The structural changes of the xCA–KCs that accompanied $CO_2$ capture and regeneration (the reverse reaction), which are represented as reaction (1) in the Introduction, were examined by XRD analysis, as shown in Figure 3-3. Figure 3-3 (a)

shows the XRD patterns of the $x$CA−KC nanocomposites after the $CO_2$ capture under moist conditions. The main diffraction peaks of $KHCO_3$ are present, verifying that the
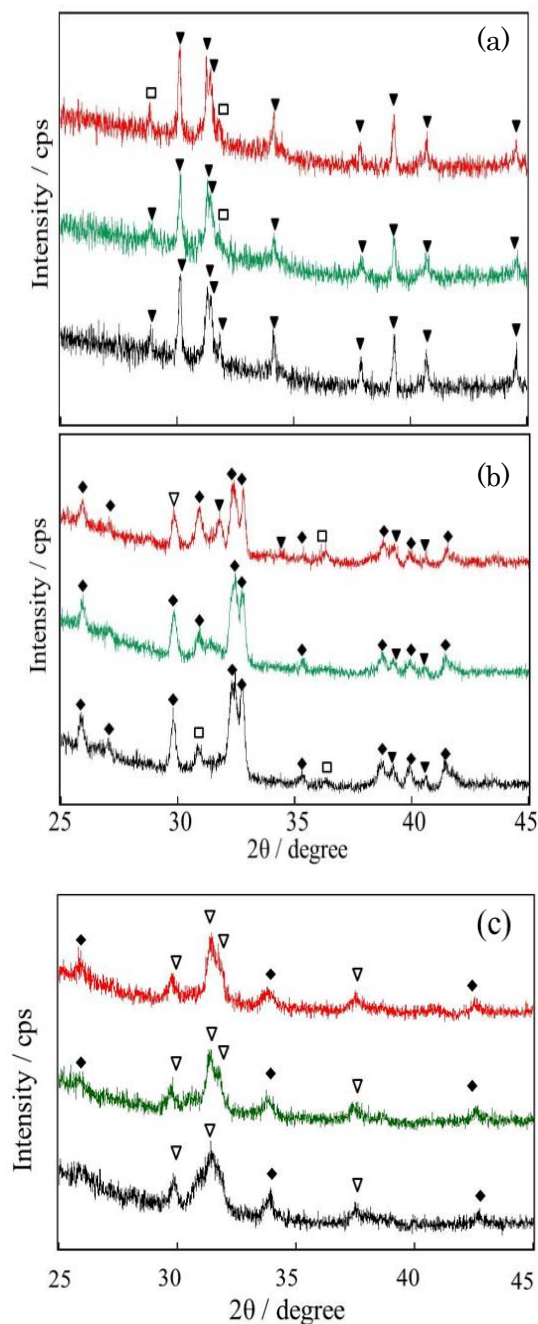


**Figure 3-3:** XRD patterns after $CO_2$ capture and regeneration: (a) xCA−KC nanocomposite after $CO_2$ capture under moist conditions; (b) xCA−KC nanocomposites placed under ambient atmosphere after being regenerated at 473 K for 2 h; (c) in situ XRD pattern of (b). Pore width: black, 7 nm; green, 16 nm; red, 18 nm. ▼: $KHCO_3$, □: $K_4H_2(CO_3)_3 \cdot 1.5H_2O$, ▽: $K_2CO_3$, ◆: $K_2CO_3 \cdot 1.5 H_2O$.

47

KHCO$_3$ nanocrystals were introduced into the mesopores of the $x$CAs through the impregnation process. Although peaks attributable to K$_4$H$_2$(CO$_3$)$_3$·1.5H$_2$O as well as to KHCO$_3$ were observed in the patterns of 16CA–KC and 18CA–KC, all the peaks in the pattern of 7CA–KC were assigned to KHCO$_3$. The patterns in Figure 3-3 (b) indicate almost complete regeneration because most of the main peaks were assigned to K$_2$CO$_3$·1.5H$_2$O instead of KHCO$_3$. This suggests that K$_2$CO$_3$ was formed by heat treatment at 473 K. Although K$_2$CO$_3$·1.5H$_2$O could be formed because of the deliquescent nature of K$_2$CO$_3$ under ambient conditions during the ex situ XRD experiment, K$_2$CO$_3$ impregnated into the mesopores of $x$CAs was exposed to the ambient atmosphere and more easily reacted with atmospheric water.

Figure 3-3 (c) is the result from in situ X-Ray diffraction experimental data, the process was elucidated in chapter 2, increasing the temperature of vacuum XRD by ribbon heater, avoiding the effect of water in the atmosphere. The main peaks could be recognized as K$_2$CO$_3$, there were still K$_2$CO$_3$.1.5H$_2$O diffraction peaks existed which may be arise from the inadequate pretreatment, all water had not been vacuumed completely. So in order to improve the procedure of in situ XRD, we could increase the time of thermal treatment, or elevate the pretreatment temperature.

3.3.3 Decomposition of xCA–KC nanocomposites

The decomposition of analytically pure potassium bicarbonate had been investigated two circles by TG-DTA, mass change to 68.6% which is approximate to theoretical value 69% after heat treatment to 473 K under the nitrogen atmosphere and the heating rate is 10 K/ min. The amount of CO$_2$ capture was decreased apparently in the second circle, and from Figure 3-4 (b) the decomposition temperature started from 423K for bulk KHCO$_3$. Figure 3-4 (c) represents the decomposed KHCO$_3$ capture CO$_2$ in the

moisture ambient, the equilibrium can be obtained after one hour which is consistent with other researches, the conversion rate is slow and cannot transit to $KHCO_3$ completely, the first circle was close to 98% of original $KHCO_3$, but the second circle was just approximate 96%.
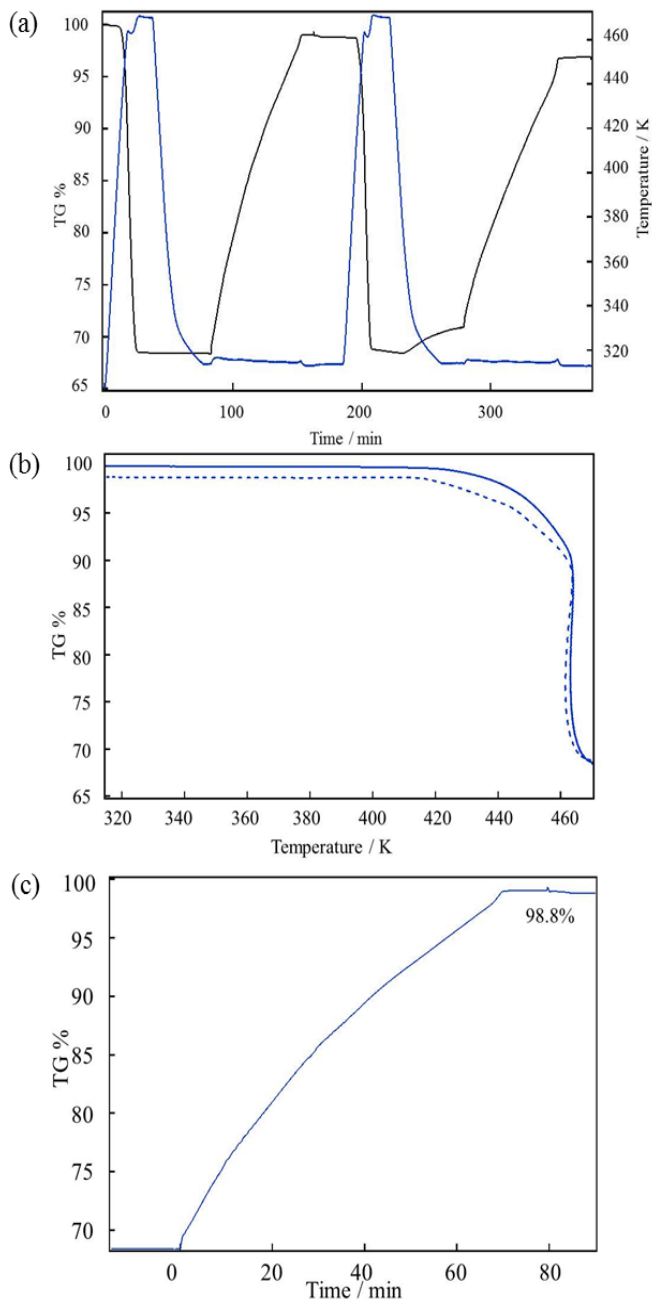


**Figure 3-4:** (a) $KHCO_3$ regeneration at 473 K in the $N_2$ atmosphere by two circles; (b)

KHCO$_3$ decomposition temperature, solid line is the first circle and dash line is the second circle; (c) CO$_2$ capture by decomposed K$_2$CO$_3$ in the moisture ambient in the first circle.

The $x$CA–KC nanocomposites were regenerated by at heating to 473 K under an N$_2$ atmosphere. The changes in weight and temperature are shown in Figure 3-5; these results reflect characteristic thermal decomposition. In the TG traces of the $x$CA–KCs, the first weight loss is attributed to the desorption of water and the second is attributed to the decomposition of KHCO$_3$ to K$_2$CO$_3$, which is accompanied by the evolution of CO$_2$ and H$_2$O. The blue line shows the decomposition process of bulk KHCO$_3$, which began to decompose at >423 K. By contrast, the $x$CA–KCs clearly decomposed at lower temperatures with decreasing pore size of the original CAs: the decomposition onset temperature decreased to 420, 390, and 380 K for 18CA–KC, 16CA–KC, and 7CA–KC, respectively. Thus, 7CA–KC exhibits an effective decrease in the required regeneration temperature. We concluded that nanocrystals of K$_2$CO$_3$ impregnated into the nanopores of CA exhibited high reactivity, resulting in easier regeneration at lower temperatures. The regeneration temperature for 7CA–KC is lower than that for other potassium-based sorbents, and the regeneration behaviors are changed when K$_2$CO$_3$ is loaded onto different sorbents, mainly depending on the properties of the support material [16].
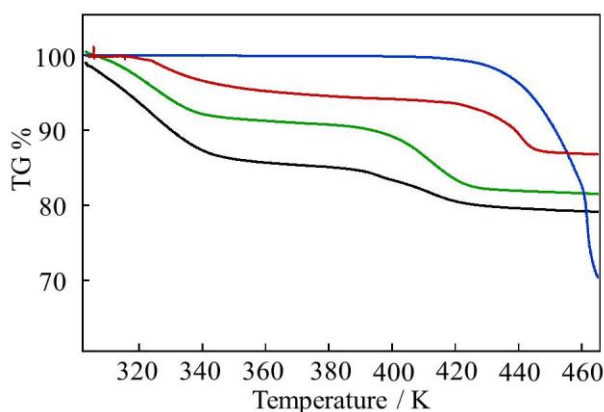
**Figure 3-5:** TG–DTA traces for the nanocomposites. Blue: $KHCO_3$, black: 7CA–KC, green: 16CA–KC, red: 18CA–KC.

3.3.4 Water adsorption

Water adsorption analysis is important for the $x$CA–KC nanocomposites because $K_2CO_3$ sorbs water from the ambient atmosphere. Zhao et al. reported that even though $K_2CO_3$– silica gel (SG) exhibits a relatively high pore volume, the total $CO_2$ sorption is only 34.5% because of the strong hygroscopicity of SG, easily leading to hydration of $K_2CO_3$ to $K_2CO_3 \cdot 1.5H_2O$ [8, 17]. This hydration should influence the $CO_2$-sorption amount of $K_2CO_3$ under moist conditions [18]. Because the $CO_2$ capture process of $x$CA–KCs involves both occlusion and physical adsorption, understanding the effects of water on $CO_2$ sorption of the original CA and the $x$CA–KCs is important. Figure 3-6 shows water sorption isotherms of $K_2CO_3$ at 303 K. Almost no water was adsorbed below a relative pressure $P/P_0$ of 0.2, whereas the sorption amount increased with increasing pressure and reached a maximum value of 9.6 mmol/g, corresponding to the water content in $K_2CO_3 \cdot 1.5H_2O$ (10.9 mmol/g). The desorption did not return to the original point because $K_2CO_3 \cdot 1.5H_2O$ hardly releases water molecules at ambient temperature, as demonstrated in the XRD experiments (Figure 3-3). Such a large hysteresis is likely observed because the hydrate formation from $K_2CO_3$ to $K_2CO_3 \cdot 1.5H_2O$ is extremely slow.

The water sorption isotherms of the CAs and $x$CA–KCs differ from those of $K_2CO_3$, as shown in Figure 3-5. Water vapor was rarely adsorbed in CAs below $P/P_0$=0.3, because the CAs are less hydrophilic than $K_2CO_3$, the physical adsorption of water is attributed to the micropores of the CAs that mesopores did not adsorb water vapor, and the saturated amount of adsorbed water was close to the micropore volume [19] [25],

thus, the three CAs should exhibit water uptake amounts corresponding to their micropore volume, as indicated in Figures 3-1 (a) and 3-7 (a) and in Table 3-1. Pore filling pressure and pore capacity depend strongly on pore width, so the 7CA shows the greatest water adsorption. Pore filling pressure was consistent with the report from McCallum et al. [24] that the material possess much smaller pore size result in pore filling occurs at a lower relative pressure. So the pore filling of 16CA occurred at a lower relative pressure than 7CA, because 16CA process more micropores which also verified by nitrogen adsorption isotherm. The desorption isotherms did not exhibit adsorption hysteresis; they returned to the starting point reversibly, as shown in Figure 3-7 (a).

By contrast, the water sorption behavior of the $x$CA–KCs was observed gradually from low relative pressure regime and more complicated because both hydration of $K_2CO_3$ and physical adsorption by the micropores of the nanocomposites contributed to water sorption. Figure 3-7(b) shows remarkable increases in the water sorption uptakes of the $x$CA–KCs in the high relative pressure region. Notably, the amounts of sorbed water were greater than the sum of the water sorption amounts of $K_2CO_3$ and CAs. This phenomenon may be attributable to the nanocrystals of $K_2CO_3$ incorporated into nanopores of the CAs being more reactive and deliquescent under high humidity conditions than bulk $K_2CO_3$. The $CO_2$ sorption isotherms of the CAs and $x$CA–KCs are shown in Figures 3-7 (c) and 3-7 (d), respectively. Because of their diminished pore volumes, all the nanocomposites exhibited smaller $CO_2$ uptake after $K_2CO_3$ impregnation, and all the $x$CA–KCs exhibited a $CO_2$ capture capacity of approximately 2.4 mmol $CO_2$/g-sorbent at 0.1 MPa. Thus, the $x$CA–KCs do not exhibit good $CO_2$ capture ability for under dry conditions.
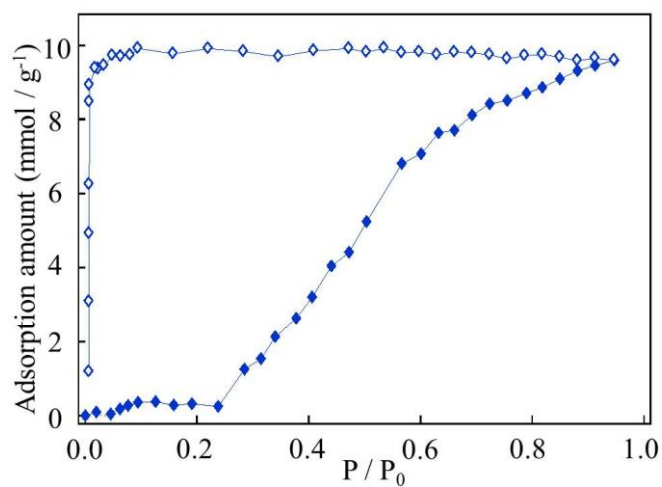
**Figure 3-6:** Water adsorption isotherms for $K_2CO_3$. Filled symbols: sorption; open symbols: desorption.
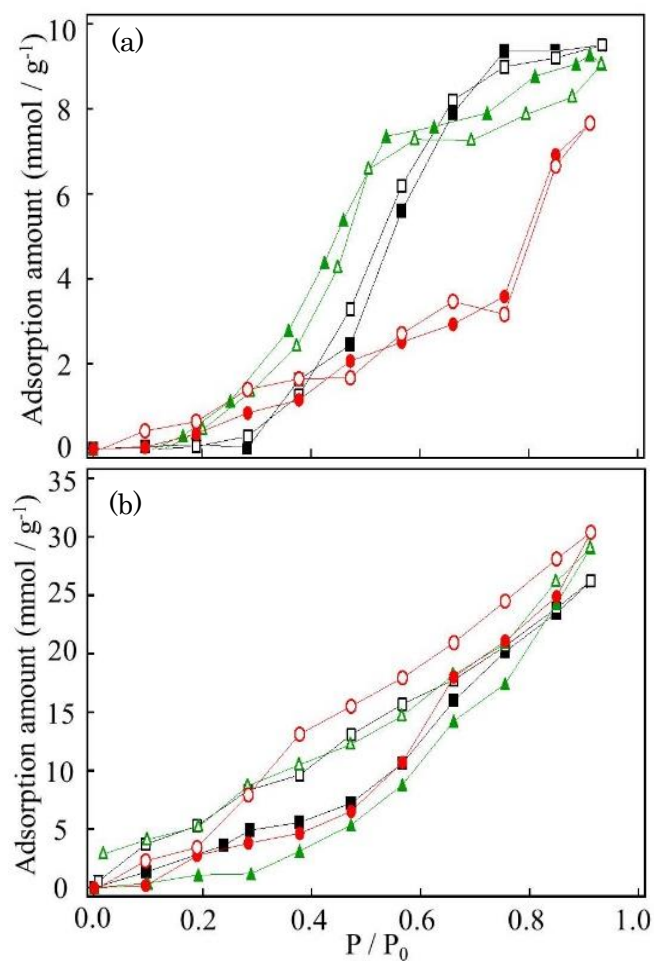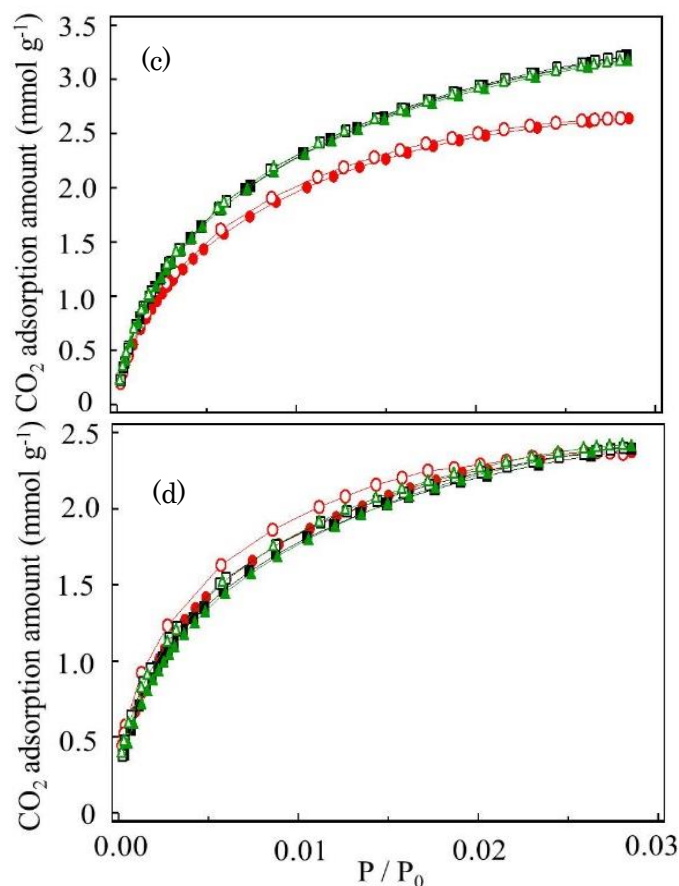
**Figure 3-7:** Water sorption and $CO_2$ sorption isotherms. Water sorption isotherms at 303 K for CAs (a) and xCA‑KCs (b). $CO_2$ adsorption isotherms at 273 K under dry conditions for CA (c) and for xCA‑KCs (d). Pore widths: black $\square$, 7 nm; green $\triangle$, 16 nm; red $\bigcirc$, 18 nm.

3.3.5 $CO_2$ capture ability under moist conditions

The amount of $K_2CO_3$ impregnated into the mesopores of CA was determined by thermogravimetry–differential thermal analysis (TG–DTA, Shimadzu DTG-60AH), where the samples were heated to 1073 K. Because the residue consisted of $K_2O$, the impregnated amounts of $K_2CO_3$ were calculated on the basis of the final TG curves to be 18.5, 21.3 and 18.8 wt% for 7CA–KC, 16CA–KC, and 18CA–KC, respectively, as

shown in Figure 3-8.
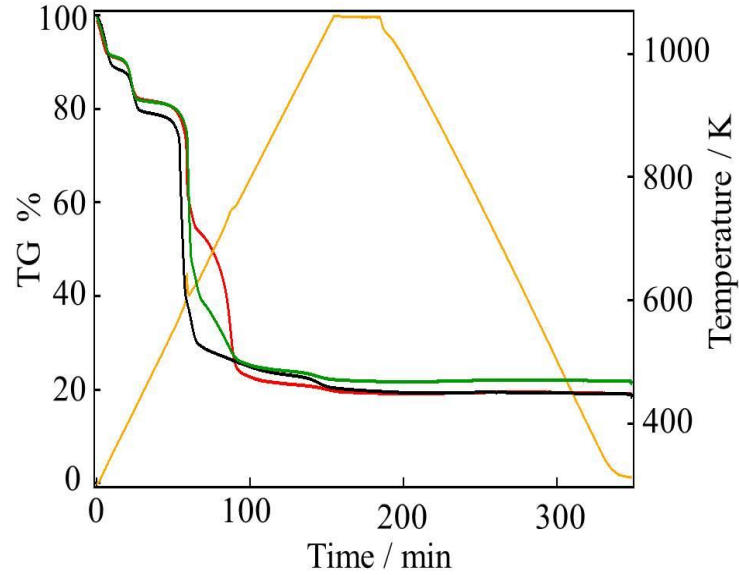


**Figure 3-8:** TG–DTA traces of xCA–KCs under $N_2/O_2$ gas flow. Black: 7CA–KC; green: 16CA–KC; red: 18CA–KC. Yellow: Temperature change.

The $CO_2$ sorption capacity of the $x$CA−KCs was calculated on the basis of their mass change resulting from reaction (3-1), one mole of $K_2CO_3$ occludes a stoichiometric amount of one mole each of $CO_2$ and $H_2O$, and the two values were calculated as the total $CO_2$ sorption capacity ($A_C$; mmol-$CO_2$/g-sorbent) and the $CO_2$ occlusion capacity of $K_2CO_3$ ($R_C$; mmol-$CO_2$/g-$K_2CO_3$). They are denoted as

$$A_C = \frac{1000\ nM_{CO_2}}{44m} \tag{3-2}$$

$$R_C = \frac{A_C}{\alpha} \tag{3-3}$$

where n (mmol) is the total amount of $CO_2$ captured, as obtained from TG data; $M_{CO_2}$ (g/mol) is the molar mass of $CO_2$, m (g) is the mass of the sorbent; and $\alpha$ is the impregnation rate of $K_2CO_3$ into the nanocomposites.

CO$_2$ sorption was conducted at 313 K at a flow rate 100 cm$^3$/min in a saturated mixed gas of CO$_2$ and water, as shown in Figure 3-9. The increase in weight (%) corresponds to the conversion of K$_2$CO$_3$ to 2KHCO$_3$. Sample 7CA–KC exhibited the greatest weight change (~17%), and bicarbonate formation reached equilibrium after 30 min for all the $x$CA–KC nanocomposites. Green et al. [20] reported that K$_2$CO$_3$ exhibits 45% CO$_2$ sorption in 100 min, and Luo et al. [11] verified that the carbonation of K$_2$CO$_3$ is low. The reaction rate of the $x$CA–KC nanocomposites was faster than that of bulk K$_2$CO$_3$, indicating the effect of nanostructured K$_2$CO$_3$.

The CO$_2$ capture capacity results are summarized in Table 3-2; the results indicate that 7CA–KC exhibits the highest CO$_2$ sorption capacity, A$_C$ = 2.68 mmol/g-sorbent (R$_C$ = 14.5 mmol/g-K$_2$CO$_3$), which is substantially higher than the theoretical amount of 7.24 mmol/g-K$_2$CO$_3$. The capture capacity results reported in Table 3-2 were estimated simply from the weight increase attributed to the sorption of CO$_2$ and H$_2$O. However,
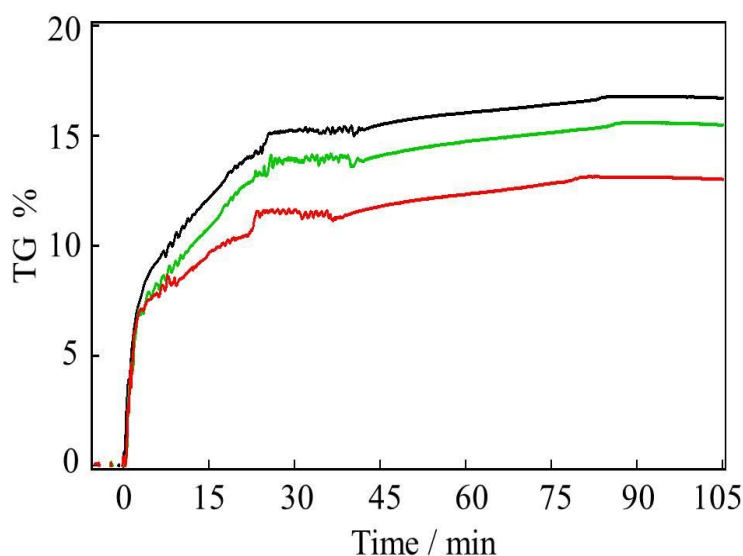


**Figure 3-9:** TG–DTA traces of carbonation reaction for xCA–KCs. Pore widths: black 7 nm; green 16 nm; red 18 nm.

the mechanism is complicated and still under study. To more precisely determine the amount of $CO_2$ captured by the $x$CA−KC nanocomposites, we used another method to measure the net amount of $CO_2$ captured, as described in section 3.3.6.

**Table 3-2:** $CO_2$ capture capacity, as measured by TG–DTA and TPD

| Composite | Loading amount | TG–DTA | | CaO soln–ppt | |
|---|---|---|---|---|---|
| | | $A_C$ | $R_C$ | $A_C$ | $R_C$ |
| 7CA−$K_2CO_3$ | 18.5 wt% | 2.68 (118) | 14.5 (638) | 2.45 (106) | 13.0 (574) |
| 16CA−$K_2CO_3$ | 21.3 wt% | 2.45 (106) | 11.4 (500) | 2.1 (91) | 9.77 (430) |
| 18CA−$K_2CO_3$ | 18.8 wt% | 2.1 (92) | 11.1 (489) | 1.7 (76) | 9.18 (404) |

$A_C$: mmol-$CO_2$/g-sorbent     (Ac): mg-$CO_2$/g-sorbent

$R_C$: mmol-$CO_2$/g-$K_2CO_3$     (Rc): mg-$CO_2$/g-$K_2CO_3$
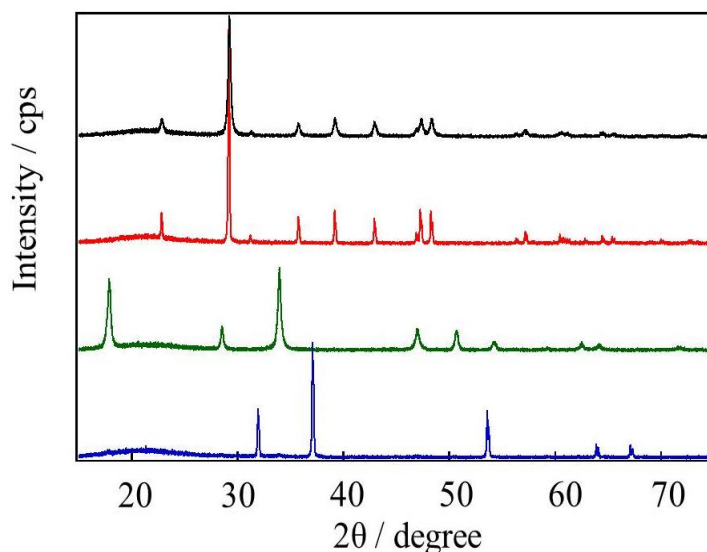


**Figure 3-10:** XRD measurement for multi-step CaO solution verification, black: the result of this study, red: CaCO3, green: Ca(OH)2, blue: CaO

3.3.6 CaO solution–precipitation method

Before the Cao solution-precipitation experiment of samples, we heated $KHCO_3$ to make $CO_2$ react with CaO solution and then did the XRD experiment to verify the resultant which is showed in Figure 3-10, the precipitation completely changed to

57

CaCO$_3$. To accurately determine the amount of CO$_2$ captured by the $x$CA–KC composites, the CaO solution–precipitation method described in experimental section 3.2.3 was used. We measured the mass of the CaCO$_3$ precipitate to estimate the CO$_2$ uptake, the results indicated sorption capacities of A$_C$ = 2.45, 2.1, and 1.7 and occlusion capacity of R$_C$ = 13.0, 9.77, and 9.18 mmol/g-K$_2$CO$_3$ for 7CA–K$_2$CO$_3$, 16CA–K$_2$CO$_3$, and 18CA–K$_2$CO$_3$, respectively, which is also reported in Table 3-2. Although the amounts of CO$_2$ uptake are lower than those obtained from the TG measurements, these are net values of CO$_2$ capture capacity. Because the impregnated amount insufficient, A$_C$ is relatively low. If the impregnation of K$_2$CO$_3$ into the mesopores of CA can be improved, more CO$_2$ will be captured and the sorbents will be easily regenerated. The values of A$_C$ and R$_C$ exhibit a dependence on the pore size of the original CA. In the case of impregnation of 7 nm mesopores of CA, a higher value of A$_C$ (per g-sorbent) is obtained. It may be because a smaller particle should be more reactive and show a higher efficiency for the CO$_2$ occlusion reaction with water vapor.
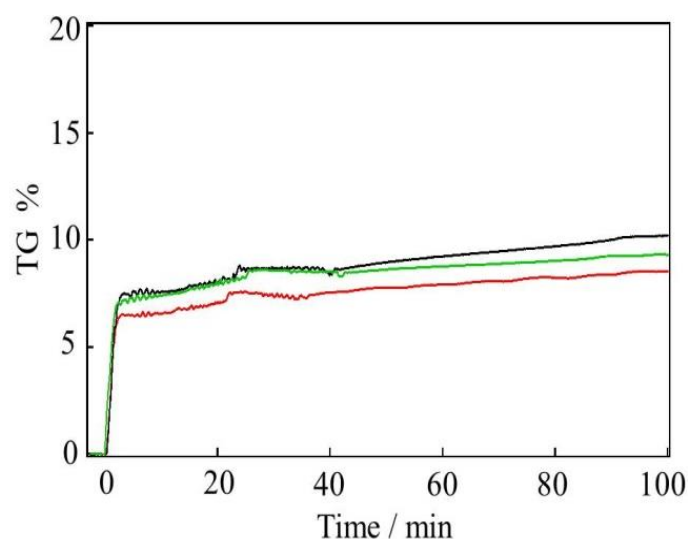


**Figure 3-11:** TG curves of the carbonation reaction of xCA. Pore widths: black 7 nm; green 16 nm; red 18 nm.

58

The $CO_2$ capture amounts are higher than the theoretical values in all $x$CA-KCs, as shown in Table 2. This can be also because the remaining pores should be efficient for chemical absorption and physical adsorption of $CO_2$ such as the formation of $H_2CO_3$ in the pores, as Figure 3-11 indicates the $CO_2$ adsorption of $x$CAs by TG-DTA under the same condition as that for the $x$CA-KCs. From this figure, the 7CA-KC is also found to possess a better $CO_2$ sorption capacity (approximate to 17% mass change) than $x$CAs.

The $CO_2$ capture amounts in the present study are excellent compared with those reported for other $K_2CO_3$-loaded composites [16, 21, 22]. Although dry potassium-based sorbents such as $K_2CO_3$–MgO exhibit excellent $CO_2$ capacities (9.0–14.9 mmol-$CO_2$/g-$K_2CO_3$) that are substantially higher than the theoretical value, these sorbents produce many other byproducts, leading to a higher temperature of 623 K for regeneration. Lee et al. [5, 21] reported that $Al_2O_3$–$K_2CO_3$ generates $KAl(CO_3)_2(OH)_2$ during the synthesis process and this byproduct does not completely convert to $K_2CO_3$ at temperatures below 563 K, and observed that $K_2CO_3$–AC and $K_2CO_3$–$TiO_2$ can be regenerated at relatively low temperatures of 473 and 403 K, respectively. However, these two composites exhibit lower $CO_2$ capture capacities of 6.5 and 6.3 mmol-$CO_2$/g-$K_2CO_3$, respectively. AC–$K_2CO_3$ is considered a promising $CO_2$ capture sorbent because of its low regeneration energy requirement and high $CO_2$ capture capacity. However, to maintain these features, $H_2O$ activation is required to convert $K_2CO_3$ to an activated form ($K_2CO_3 \cdot 1.5H_2O$) [18]. $ZrO_2$–$K_2CO_3$ has a capacity of 6.2–6.9 mmol-$CO_2$/g-$K_2CO_3$ when the reaction temperature within 323–333 K under an ambient atmosphere of 9% $H_2O$, 1% $CO_2$, and balance $N_2$ [5, 23].

3.3.7 The cycling of 7CA-KC composites

7CA-KCs shows the lowest regeneration temperature and highest $CO_2$ capture

capacity. Cyclabilty of 7CA-KC in the adsorption / desorption were studied to check the stability for 3 cycles of sorption/desorption, as show in Figure 3-12. The results showed that the regeneration temperature was 20 K higher than the first cycle but retained a similar temperature for the second and third cycles, which is still lower than that of bulk $KHCO_3$. We repeated the TG decomposition experiment in the first cycle by using a fresh sample, and found that the result was reproducible. The blue and yellow line in Figure 3-13 were the first and second carbonation of the fresh sample 7CA-KC, respectively. The results indicate in the $CO_2$ capture under moist conditions, the uptake amount was decreased gradually with the cycle number but still higher than the theoretical value of $K_2CO_3$.

In order to study the reason that the $CO_2$ capture amount was decreased in the adsorption / desorption process, we compared the porosity of 7CA-KC after the third cycle with that of the original sample by the $N_2$ adsorption measurement. We found that the specific surface area and micropore volume a little decreased after the third cycle in Figure 3-14. This may be attributed to sintering of nanoparticles of $K_2CO_3$. In order to avoid this behavior, we will improve the preparation condition of composites.
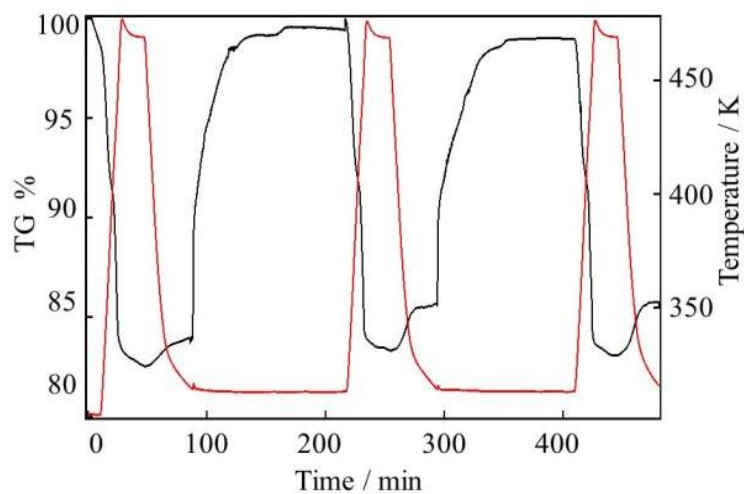


**Figure 3-12:** TG–DTA curves of 3 cycles for 7CA-KC.

60
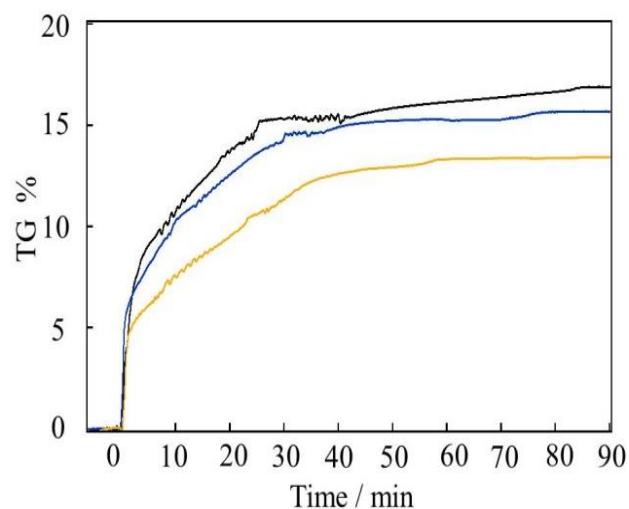
**Figure 3-13:** TG–DTA curves of carbonation reaction for 7CA–KCs. Black: the data from 7CA-KC; Blue: the first adsorption of fresh sample; yellow: the second adsorption of fresh cycle.
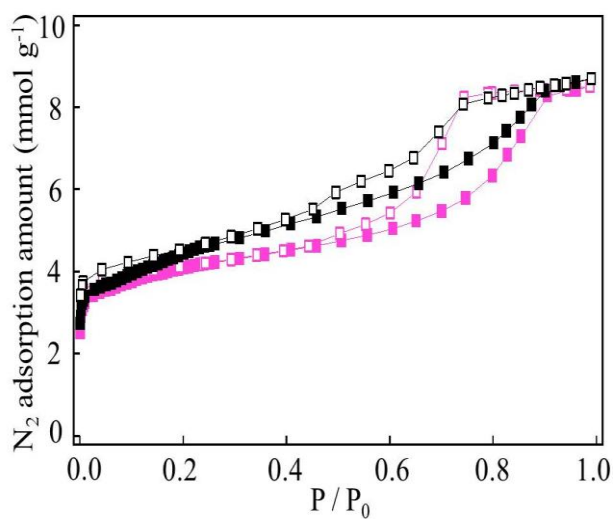


**Figure 3-14:** $N_2$ adsorption isotherms of 7CA-KC. black, the first circle of 7CA-KC; pink, the third circle of 7CA-KC

## 3.4 Conclusion

CA–$K_2CO_3$ nanocomposites ($x$CA–KC) were prepared by impregnation of $K_2CO_3$ nanocrystals into the mesopores of three CAs with different pore sizes of 7, 16, and 18

nm for the development of an excellent $CO_2$ sorbent with a high capacity, high selectivity, and low energy cost for regeneration. The performance of the nanocomposites is attributed to both chemical and physical capture being involved in the $CO_2$ capture. The $x$CA–KCs can be completely regenerated at temperatures below 423 K; 7CA–$K_2CO_3$ in particular exhibited excellent results, where regeneration began at 390 K and was completed at 420 K. These results were attributed to the high reactivity of nanostructured $K_2CO_3$, which rendered the $K_2CO_3$ crystals unstable and reduced the regeneration temperature. These $x$CA–KC nanocomposites exhibited excellent $CO_2$ capture capacity and can be considered a promising material for $CO_2$ capture from the viewpoints of economic effectiveness and energy efficiency. We also concluded that CAs can be used as a porous support for the preparation of nanocomposites with low sorbent regeneration temperatures. There are some disadvantages such as the instability of decomposition temperature in the adsorption / desorption cycles, and the adsorption amount was decreased with the cycle number. So we think it is important to overcome these drawbacks in the further research to become a potential adsorbent for $CO_2$ capture.

## References

[1] J. Wang, L. Huang, R. Yang, Z. Zhang, J. Wu, Y. Gao, Q. Wang, D. O'Hare and Z. Zhong, Recent advances in solid sorbents for $CO_2$ capture and new development trends, Energy & Environmental Science, 2014, 7, 3478–3518.

[2] Q. Wang, J. Luo, Z. Zhong, and A. Borgna, $CO_2$ capture by solid adsorbents and their applications: current status and new trends, Energy & Environmental Science, 2011, 4, 42–55.

[3] S. C. Lee, Y. M. Kwon, C .Y. Ryu, H. J. Chae, D. Ragupathy, S. Y. Jung, J. B. Lee, C. K. Ryu, and J. C. Kim, Development of new alumina-modified sorbents for $CO_2$ sorption and regeneration at temperatures below 200℃, Fuel, 2011, 90(4), 1465–1470.

[4] S.-W. Park, D.-H. Sung, B.-S. Choi, J.-W. Lee, and H. Kumazawa, Carbonation kinetics of potassium carbonate by carbon dioxide, Journal of Industrial and Engineering Chemistry, 2006, 12(4), 522–530.

[5] S. C. Lee and J. C. Kim, Dry potassium-based sorbents for $CO_2$ Capture, Catalysis Surveys Asia, 2007, 11(4), 171–185.

[6] N. N. A. H. Meis, A. M. Frey, J. H. Bitter, and K. P. de Jong, Carbon nanofiber-supported $K_2CO_3$ as an efficient low-temperature regenerable $CO_2$ sorbent for post-combustion capture, Industrial & Engineering Chemistry Research, 2013, 52(36), 12812–12818.

[7] B.-T. Zhang, M. Fan, and A. E. Bland, $CO_2$ separation by a new solid K–Fe sorbent, Energy &Fuels, 2011, 23, 1919–1925.

[8] C. Zhao, X. Chen, and C. Zhao, $CO_2$ adsorption using dry potassium-based sorbents with different supports, Energy Fuels, 2009, 23, 4683–4687.

[9] C. Zhao, X. Chen, and C. Zhao, Carbonation and Active-component-distribution

behaviors of several potassium-based sorbents, Industrial & Engineering Chemistry Research, 2011, 50(8), 4464–4470.

[10] H. Chioyama, H. Luo, T. Ohba, and H. Kanoh, Temperature-dependent double-step $CO_2$ occlusion of $K_2CO_3$ under moist conditions, Adsorption Science & Technology, 2015, 33(3), 243–250.

[11] H. Luo, H. Chioyama, S. Thürmer, T. Ohba, and H. Kanoh, Kinetics and structural changes in $CO_2$ capture of $K_2CO_3$ under a moist condition, Energy & Fuels, 2015, 29(7), 4472–4478.

[12] R. W. Pekala and C. T. Alviso, Carbon aerogels and xerogels, Material Research Society Symposium process, 1992, 270, 3–14.

[13] R. W. Pekala, C. T. Alviso, F. M. Kong, and S. S. Hulsey, Aerogels derived from multifunctional organic monomers, Journal of Non-Crystalline Solids, 1992, 145, 90–98.

[14] S. J. Taylor, M. D. Haw, J. Sefcik, and A. J. Fletcher, Gelation mechanism of resorcinol–formaldehyde gels investigated by dynamic light scattering, Langmuir, 2014, 30(34), 10231–10240.

[15] D. Fairen-Jimenez, F. Carrasco-Marin, and C. Moreno-Castilla, Porosity and surface area of monolithic carbon aerogels prepared using alkaline carbonates and organic acids as polymerization catalysts, Carbon, 2006, 44(11), 2301–2307.

[16] C. Zhao, X. Chen, and C. Zhao, $K_2CO_3/Al_2CO_3$ for capturing $CO_2$ in flue gas from power plants.Part2: Regeneration Behaviors of $K_2CO_3/Al_2O_3$,Energy & Fuels, 2012, 26, 1406–1411.

[17] C. Zhao, X. Chen, E. J. Anthonyb, X. Jiang, L. Duana, Y. Wu, W. Dong, and C. Zhao, Capturing $CO_2$ in flue gas from fossil fuel–fired power plants using dry

regenerable alkali metal-based sorbent, Progress in Energy and Combustion Science, 2013, 39(6), 515–534.

[18] C. Zhao, X. Chen, C. Zhao, and Y. Liu, Carbonation and hydration characteristics of dry potassium -based sorbents for $CO_2$ capture, Energy& Fuels, 2009, 23, 1766–1769.

[19] Y. Hanzawa and K. Kaneko, Lack of a predominant adsorption of water vapor on carbon mesopores, Langmuir, 1997, 13(22), 5802–5804.

[20] D. A. Green, B. S. Turk, J. W. Portzer, R. P. Gupta, W. J. McMichael, Y. Liang, T. Moore, and D. P. Harrison, Carbon dioxide capture from flue gas using dry regenerable sorbents, Quarterly Technical Progress Report, 2003.

[21] S. C. Lee, B. Y. Choi, T. J. Lee, C. K. Ryu, Y. S. Ahn, and J. C. Kim, $CO_2$ absorption and regeneration of alkali metal-based solid sorbents, Catalysis Today, 2006, 111,(3-4), 385–390.

[22] S. C. Lee, H. J. Chae, S. J. Lee, B. Y. Choi, C. K. Yi, J. B. Lee, C. K. Ryu, and J. C. Kim, Development of regenerable MgO-based sorbent promoted with $K_2CO_3$ for $CO_2$ capture at low temperatures, Environmental Science & Technology, 2008, 42(8), 2736-2741.

[23] S. C. Lee, H. J. Chae, S. J. Lee, Y. H. Park, C. K. Ryu, C. K. Yi, and J. C. Kim, Novel regenerable potassium-based dry sorbents for $CO_2$ capture at low temperatures, Journal of Molecular Catalysis B: Enzymatic, 56 (2-3), 179–184.

[24] C. L. McCallum, T. J. Bandosz, S. C. McGrother, E. A. Müller, and K. E. Gubbins, A molecular model for adsorption of water on activated carbon: comparison of simulation and experiment, Laugmuir, 1999, 15, 533-544.

[25] K. Kaneko, Y. Hanzawa, T. Iiyama, T. Kanda, and T. Suzuki, Cluster-mediated

water adsorption on carbon nanopores, Adsorption, 1999, 5, 7-13.

[26] M-F Yan, L-H Zhang, R. He, Z-F Liu, Synthesis and characterization of carbon aerogels with different catalysts, Journal of Porous Materials, 2015, 22(3), 699-703.

# Chapter 4:CO$_2$ capture by activated carbon fibers– potassium carbonate nanocomposites

## 4.1 Introduction

Activated carbon fiber (ACF) is one of the most important carbon nanoporous materials, because it possesses many advantages over other commercial porous materials such as very high surface area and pore volume, chemical inertness, good mechanical stability, and possess a larger adsorption capacity and greater rate of adsorption-desorption process. ACF is a promising microporous material with a fiber morphology (Figure4-1), quite pure because of low quantity of inorganic impurities and well-defined porous structure with uniform slit-shape pores [1, 2]. So they can be used in various applications, like polarizable electrodes, catalysis applications, CO$_2$ capture [13], SOx and NOx removal, gas separation, cigarette filters, water purification and molecular sieves. The applications in the gas phase are mainly due to the porous structure [3].
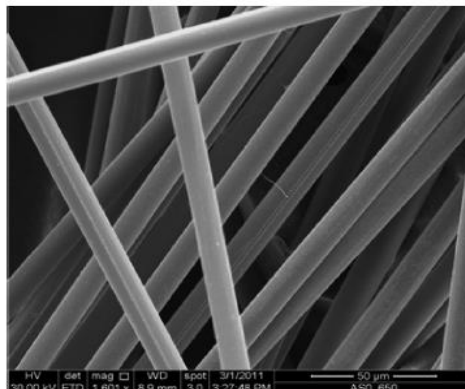


**Figure 4-1:** SEM images of the surface of activated carbon fibers [4]

Just as showed in Figure 4-2, Activated carbon fiber (ACF) is the combination of

activated carbon and carbon fibers, in producing carbon fibers adding a thermal treatment. ACFs are generally fabricated from pitches, celluloses, phenol resin and polyacrylonitrile resin, and the selection of precursor carbon fiber, activation method and experimental conditions play an important role for tailoring pore size distribution and porous structures. Compare to other porous material such as silicas, zeolites whose $CO_2$ capacity will be hinder by the presence of water and metal-organic frameworks (MOF). ACF provide properties like low cost, a high hydrophobicity, and chemical stability [5].
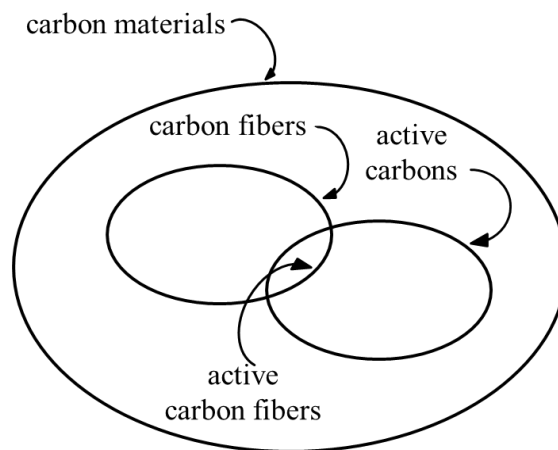


**Figure 4-2:** The classification of activated carbon fibers among carbon materials [6].

ACF could be used as porous substrate by tailoring their surface chemistry and porous texture to form nanocomposites, adapting to some explicit applications. Guo et al. reported that impregnated $TiO_2$ on ACF to enlarge the visible light photocatalytic activity [7]. Sun et al. modified ACFs with carbon nanotubes (CNTs) to capture dye through the electrochemical degradation [8], and Kitagawa et al. also reported $CO_2$ capture by ACFs in the proceedings of Nippon Kagakukai. N-enriched activated carbon fibers have been used as $CO_2$ adsorbents, and get a high uptake 3.4 mmol $CO_2$/g at 25℃

and 1atm [5]. Shen et al. also reported the hierarchical activated carbon fibers for $CO_2$ capture, and this material possessed a high surface area above 2000 $m^2/g$, showed the excellent $CO_2$ capture amount in the moisture ambience (7.0 mmol/g and 4.8 mmol/g at 273 K and 298 K) [13]. In recent years, in order to enlarge the performance for porous materials, various surface modification studies have been extensively researched, such as nitrogen-doped, cation exchange, amine-modified method. The influence of nitrogen doping on the porous structure had been investigated, and verified that $CO_2$ capture capacities (1.9-3.5 mmol$CO_2$/g) of N-doped fibers were twice higher than then N-free fibers [14]. Bai et al. demonstrated that introduced oxygen-containing functional groups such as carboxylic and hydroxyl groups by liquid oxidation to increase $CO_2$ capture amount, the mechanism presented in Figure 4-3 $CO_2$ molecules were appealed to the surface groups because of the electron-rich properties that generated attractive forces with electrons in the $CO_2$ molecules [15]. In this research, we loaded $K_2CO_3$ into ACFs, even though this process would lead to a severe decrease in surface area, pore volume like amine modification whose $CO_2$ capture capacity dramatically decreased after incorporation, but we think the chemical adsorption of $CO_2$ will compensate the loss of structure change. So in this study, in addition to fabricate the CA-KC composites, we also investigated the ACF composites for $CO_2$ capture by impregnating $K_2CO_3$ to ACF-W15. ACF-15 is a kind of commercial material whose specific surface area is 1275 $m^2/g$, total pore volume approximate 1.2 $m^2/g$, and the average pore size is 3.2 nm.
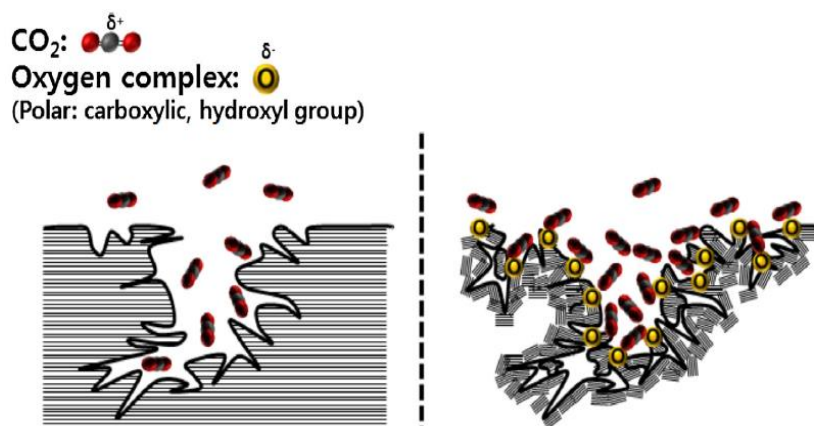
**Figure 4-3:** mechanism for the $CO_2$ adsorption properties of liquid-oxidized activated carbon fiber [15].

## 4.2 Experimental Section

4.2.1 Preparation of ACF–potassium carbonate (KC) nanocomposites

Before the preparation of composites, activated carbon fibers had been grinded into granule in order to facilitate the impregnating process. ACF–KC nanocomposites were prepared by impregnating the nanopores of the ACFs with a 0.15 mol/dm$^3$ K$_2$CO$_3$ (99.5% chemical purity) aqueous solution [9]. The mixture was then stirred with a magnetic stirrer for 24 h at room temperature. The aqueous solution was dried at 378 K in a vacuum evaporator. The samples were subsequently dried again in a furnace under an Ar ambient atmosphere at 573 K for 2 h. The nanocomposites are denoted as ACF–KC.

4.2.2 Measurements and characterization

The porosities of the ACF-W15 and the ACF–KC nanocomposite were characterized by N$_2$ adsorption at 77 K using an Autosorb-MP1 (Quantachrome Instruments). CO$_2$ adsorption was measured using a Belsorp-Mini (MicrotracBEL Corp.). The ACF and ACF–KC nanocomposite were pretreated by heating to 423 K under vacuum for 2 h

70

before the gas adsorption measurements because $K_2CO_3$ is partially converted into KHCO$_3$ under an ambient atmosphere containing $CO_2$ and $H_2O$. Water adsorption isotherms were obtained by a gravimetric method at 303 K, the equilibration time was 2 h.

The Brunauer–Emmett–Teller (BET) method was used to analyze the specific surface areas ($S_{BET}$) on the basis of linear plots over the relative pressure ($P/P_0$) range 0.05–0.35 for the $N_2$ adsorption isotherm data. The total volume was obtained at a relative pressure of 0.99, and the Dubinin–Radushkevich equation was used to calculate the micropore volume. The mesopore diameters were estimated by the Barrett-Joyner-Halenda method.

The amount of $K_2CO_3$ impregnated into the mesopores of CA was determined by thermogravimetry–differential thermal analysis (TG–DTA, Shimadzu DTG-60AH), where the samples were heated to 1073 K, just as introduced in chapter 3. The loading amount was determined as 18.5 %.

After the ACF–KC nanocomposite was heated to 473 K at 10 K/min under an $N_2$ atmosphere and maintained at 473 K for 5 min to ensure complete formation of $K_2CO_3$, the temperature was decreased to 313 K, and $CO_2$ and $H_2O$ were introduced into the sample chamber of the TG–DTA apparatus for 2 h by flowing $CO_2$ through distilled water. The ACF–KC nanocomposite reacted with $CO_2$ and $H_2O$ to form ACF–KHCO$_3$. The crystal structures before and after the $CO_2$ capture were measured through ex situ X-ray diffraction (XRD) on an X-ray diffractometer (MAC Science, M03XHF) equipped with a Cu $K\alpha$ radiation source (40 kV, 25 mA, $\lambda = 0.15406$ nm). We heated the ACF–KHCO$_3$ nanocomposites to 473 K in order to study the regeneration process under the same conditions used in the aforementioned experiments.

## 4.3 Results and Discussion

4.3.1. BET surface area and pore size distributions (PSDs) of the ACF and ACF–KC
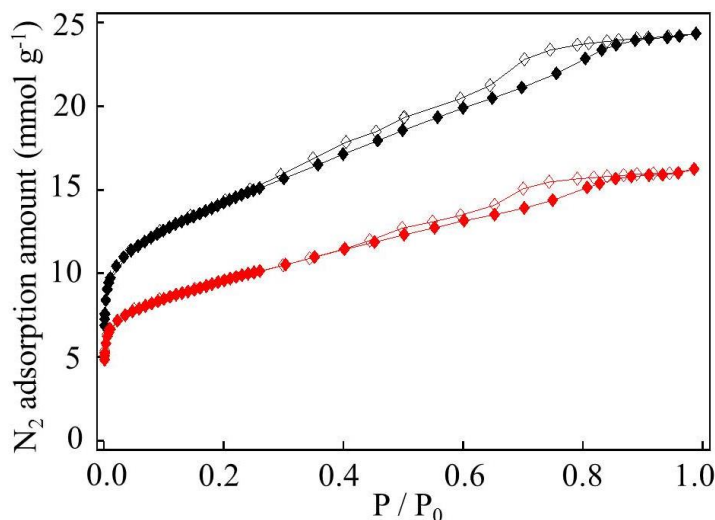


**Figure 4-4:** $N_2$ adsorption isotherms at 77 K under dry conditions for ACF-W15 and ACF–KC. Black: ACF, red: ACF-KC

The pore structures were characterized using $N_2$ adsorption isotherms volumetrically measured at 77 K after pretreatment at 423 K for 2 h; the obtained isotherms are presented in Figure 4-4 ACF-W15 has the saturated amount of adsorption over 24 mmol/g, possesses a clear hysteresis loop close to the IUPAC H2, verifying ACF-W15 has a mesoporous structure in addition to the microporous. The adsorption amount of ACF with smaller pore width should possess a larger uptake in the low relative pressure region, however Figure 4-4 showed that ACF-W15 without a high uptake amount in the low pressure, from other dissertation [10] we can consider this nanomaterial has a larger micropores relatively. In this study, the $N_2$ adsorption amount decreased after $K_2CO_3$ impregnation treatment ($S_{BET}$ reduced from 1123 to 758 $m^2$/g and $V_{mic}$ decreased from 0.43 to 0.29 $cm^3$/g), indicating that $K_2CO_3$ was successfully incorporated into the

micropores and mesopores of the ACF-W15.

4.3.2. Structural changes induced by $CO_2$ capture and regeneration

The structural changes of the ACF–KC that accompanied $CO_2$ capture and regeneration were examined by XRD analysis, as shown in Figure 4-5. The black line shows the XRD patterns of the ACF–KC nanocomposite after the $CO_2$ capture under moist conditions. The diffraction peaks of $KHCO_3$ are present, verifying that the $KHCO_3$ nanocrystals were introduced into the mesopores of the ACF-W15 through the impregnation process. The red line presented the XRD pattern after regeneration, indicating almost complete regeneration because most of the main peaks were assigned to $K_2CO_3 \cdot 1.5H_2O$ instead of $KHCO_3$. This suggests that $K_2CO_3$ was formed by heat treatment at 473 K. Although $K_2CO_3 \cdot 1.5H_2O$ could be formed because of the deliquescent nature of $K_2CO_3$ under ambient conditions during the ex situ XRD experiment, $K_2CO_3$ impregnated into the mesopores of ACF which possess a high specific surface area was exposed to the ambient atmosphere and more easily reacted with atmospheric water.
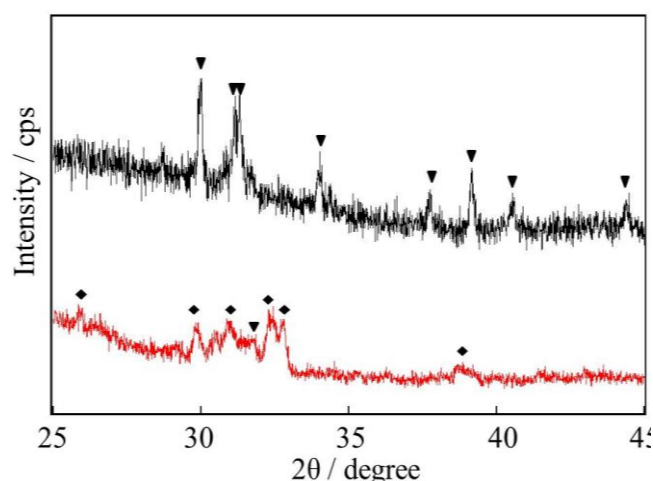


**Figure 4-5:** XRD patterns after $CO_2$ capture and regeneration: black, ACF-KC after $CO_2$ capture under moist conditions; red, ACF-KC nanocomposite placed under ambient

atmosphere after being regenerated at 473 K for 2 h. ▼: $KHCO_3$, □: $K_4H_2(CO_3)_3 \cdot 1.5H_2O$, ▽: $K_2CO_3$, ◆: $K_2CO_3 \cdot 1.5 H_2O$.

4.3.3 Decomposition of ACF–KC nanocomposites

The ACF-KC nanocomposite was regenerated by at heating to 473 K under an $N_2$ atmosphere. Figure 4-6 showed the changes in weight and temperature of $x$CA–KCs and ACF-KC. In the TG traces, the first weight loss is attributed to the desorption of water and the second is attributed to the decomposition of $KHCO_3$ to $K_2CO_3$, which is accompanied by the evolution of $CO_2$ and $H_2O$. The blue line shows the decomposition process of bulk $KHCO_3$, which began to decompose at >423 K. Even through ACF-KC started to decompose at a lower temperature than bulk $KHCO_3$, it is still higher than the 16CA-KC and 7CA-KC composites, and just as showed in Figure 5-5, ACF-KC started to decompose at 420K and finish at 440K.
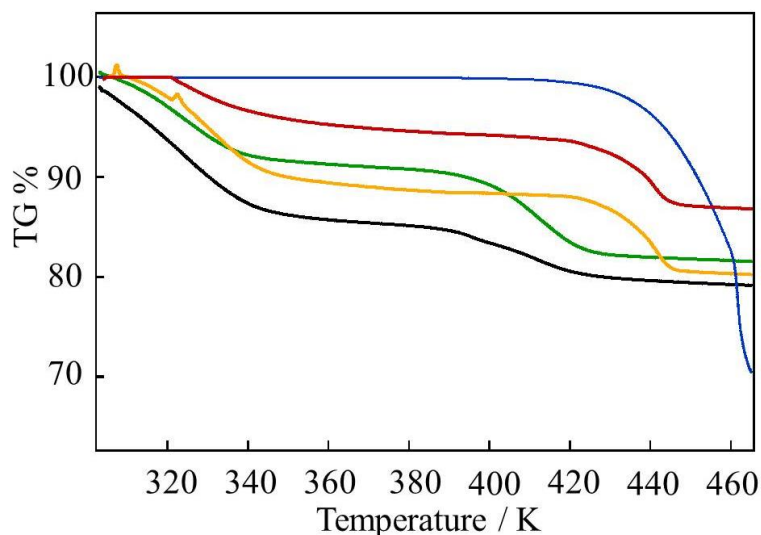


**Figure 4-6:** TG–DTA traces for the nanocomposites. Blue: $KHCO_3$, black: 7CA–KC, green: 16CA–KC, red: 18CA–KC, yellow: ACF-KC.

### 4.3.4. Water adsorption

Figure 4-7 shows water sorption isotherms of ACF and ACF-KC at 303 K. the black line represented the ACF, which has a small water adsorption at the low relative pressure and the sorption amount increased with increasing pressure, the total value of water adsorption is above 40 mmol/g. Monge et al. reported the position of the beginning of the isotherm and the knee are located at lower values of relative pressure the smaller the micropore size [2]. There was no obvious hysteresis was observed which is differ from those of $K_2CO_3$ adsorption isotherm (chapter 3). The desorption isotherms did not exhibit adsorption hysteresis, and returned to the starting point reversibly. By contrast, the water sorption behavior of the ACF–KC was more complicated because both hydration of $K_2CO_3$ and physical adsorption by the micropores of the nanocomposites contributed to water sorption. The desorption did not return to the original point because $K_2CO_3 \cdot 1.5H_2O$ hardly releases water molecules at ambient temperature, as demonstrated in the XRD experiments in chapter 4. Red line showed the ACF-KC water adsorption whose result was reverse to the xCA–KCs composites, because there was a remarkable increase in the water sorption uptakes of the xCA–KCs in the high relative pressure region which was discussed in the previous chapter. However, ACF-KC composite showed decreased uptake amount, this phenomenon may be attributable to the great reduce of $V_{mic,}$ which is more effective than the deliquescent property of $K_2CO_3$.
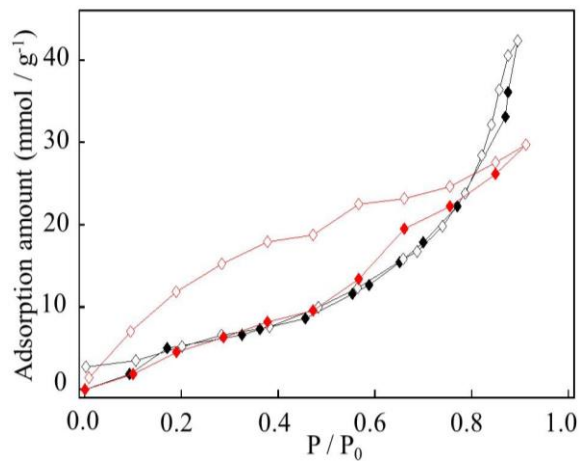
**Figure 4-7:** Water adsorption isotherms for ACF (black) and ACF-KC (red). Filled symbols: sorption; open symbols: desorption.
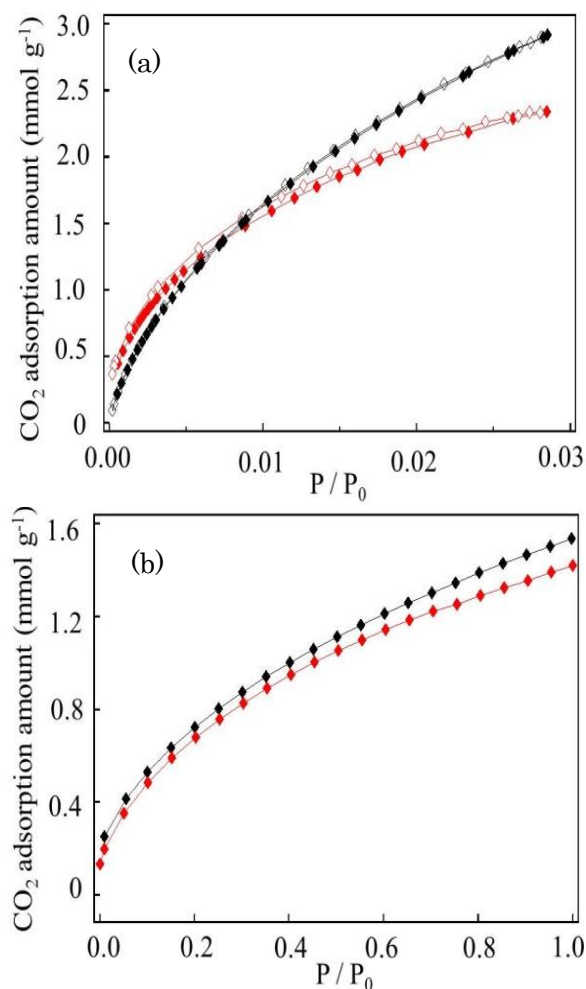


**Figure 4-8:** $CO_2$ adsorption isotherms at 273 K (a) and 313K (b) under dry conditions, black: ACF, red: ACF-KC

4.3.5 $CO_2$ adsorption

The $CO_2$ sorption isotherms of the ACF and ACF–KC at 273K (a) and 313K (b) are showed in Figure 4-8 respectively. The reduction of pore volumes, lead to the smaller $CO_2$ uptake after $K_2CO_3$ impregnation in the 273K. ACF-KC exhibited a $CO_2$ capture capacity of approximately 2.0 mmol $CO_2$/g-sorbent at 0.1 MPa. Which elucidated it does not exhibit good $CO_2$ capture ability under dry conditions. The result in the 313K showed the same trend, the amount of uptake is higher for ACF. However, the total water adsorption for 313K is less than 273K.

4.3.6 $CO_2$ capture ability under moist conditions

The $CO_2$ sorption capacity of the ACF-KC was calculated on the basis of their mass change resulting from reaction (3-1): one mole of $K_2CO_3$ occludes a stoichiometric amount of one mole each of $CO_2$ and $H_2O$, and the two values were calculated as the total $CO_2$ sorption capacity (AC; mmol-$CO_2$/g-sorbent) and the $CO_2$ occlusion capacity of $K_2CO_3$ (RC; mmol-$CO_2$/g-$K_2CO_3$). The calculation was used equation (3-2) and (3-3) which were detailed interpreted in the chapter 3.

$CO_2$ sorption was conducted at 313 K and 323K at a flow rate 100 cm$^3$/min in a saturated mixed gas of $CO_2$ and water, respectively. The black line presented 313K, and red line showed the results of 323K. The increase in weight (%) corresponds to the conversion of $K_2CO_3$ to $2KHCO_3$. Sample ACF-KC exhibited the high weight change (~15%) which was smaller than 7CA-KC, and bicarbonate formation reached equilibrium after 40 min. Ever through bicarbonate rate is higher than bulk $K_2CO_3$[11, 12], it is still lower than xCA–KC nanocomposites in this study. The $CO_2$ capture capacity results are summarized in Table 4-1, the results indicated that with the increase

of temperature the $CO_2$ adsorption amount was decreased which in accordance with other researches. ACF-KC exhibited the higher $CO_2$ sorption capacity in 313K, $A_C$ = 2.56 mmol/g-sorbent, the loading amount was 18.5 wt % calculated by the same way in the chapter 3. So $R_C$ = 13.8 mmol/g-$K_2CO_3$, the capture value was substantially higher than the theoretical amount of 7.24 mmol/g-$K_2CO_3$.
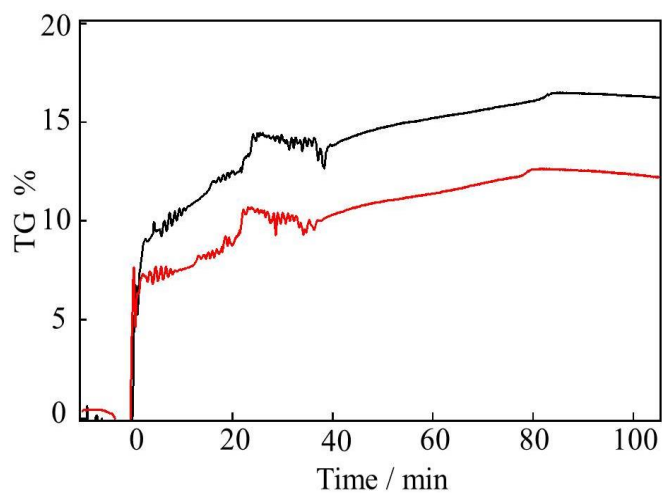


**Figure 4-9:** TG–DTA traces of carbonation reaction for ACF–KCs at 313K (black) and 323K (red).

**Table 4-1:** $CO_2$ capture capacity for ACF-KC at 313K and 323K

| ACF-KC           Temperature | $A_C$ (mmol $CO_2$ / g sorbent) | $R_C$ (mmol $CO_2$ / g $K_2CO_3$) |
|---|---|---|
| 313K | 2.56 (113) | 13.8 (610) |
| 323K | 1.9 (85) | 10.4 (459) |

$A_C$: mmol-$CO_2$/g-sorbent    ($A_C$): mg-$CO_2$/g-sorbent

$R_C$: mmol-$CO_2$/g-$K_2CO_3$    ($R_C$): mg-$CO_2$/g-$K_2CO_3$

## 4.4 Conclusion

In this chapter, we investigated the characterization of ACF-W15 and ACF-KC by nitrogen adsorption isotherm, the specific surface area and micropore value were decreased dramatically after incorporate $K_2CO_3$ into ACF. In the result of TG-DTA, ACF-KC composite changed to a lower start decomposition temperature than bulk $KHCO_3$ and possessed a higher bicarbonate rate than $K_2CO_3$ ascribed to the $K_2CO_3$ loading. However, it was still less effectivity than 7CA-KC composite whose decomposition temperature started at 380 K and finished at 420 K. The $CO_2$ capture capacity is 13.8 mmol $CO_2$ / g $K_2CO_3$ higher than the theoretical value of $K_2CO_3$ and 16CA-KC, 18CA-KC. So we think the pore width play an important role in composites material, and the $CO_2$ capture amount was highly depend on the properties of matrix.

# References

[1] T. Lee, C-H. Ooi, R. Othman, F-Y. Yeoh, Activated carbon fiber- the hybrid of carbon fiber and activated carbon, Reviews on Advanced Materials Science, 2014, 36, 118-136.

[2] J. Alcan˜iz-Monge, A. Linares-Solano, B. Rand, Mechanism of adsorption of water in carbon micropores as revealed by a study of activated carbon fibers, The Journal of Physical Chemistry B, 2002, 106, 3209-3216.

[3] J.M. Valente Nabais, P. J. M. Carrott, Chemical characterization of activated carbon fibers and activated carbons, Journal of Chemical Education, 2006, 83(3), 436-438.

[4] M. B. Va'zquez-Ssantos, F. Sua'rez-Garci'a, A. Marti'nez-Alonso, J. M. D. Tasco'n, Activated carbon fibers with a high heteroatom content by chemical activation of PBO with phosphoric acid, Langmuir, 2012, 28, 5850-5860.

[5] N. Di'ez, P. A'lvarez, M. Granda, C. Blanco, R. Santamari'a, R. Mene'ndez, N-enriched ACF from coal-based pitch blended with urea-based resin for $CO_2$ capture, Microporous and Mesoporous Materials, 2015, 201, 10-16.

[6] T. J. Mays, Chapter 3- Active Carbon Fibers (Elsevier Science Ltd, Oxford, 1999).

[7] X. Guo, J. Dai, K. Zhang, X. Wang, Z. Cui, J. Xiang, Fabrication of N-doped TiO / activated carbon fiber composites with enhanced photocatalytic activity, Textile Research Journal, 2014, 13, doi: 10.1177/0040517514532159.

[8] Y. Sun, G. Wang, Q. Dong, B. Qian, Y. Meng, J. Qiu, Electrolysis removal of methyl orange dye from water by electrospun activated carbon fibers modified with carbon nanotubes, Chemical Engineering Journal, 2014, 253, 73-77.

[9] S. C. Lee, Y. M. Kwon, C .Y. Ryu, H. J. Chae, D. Ragupathy, S. Y. Jung, J. B. Lee, C. K. Ryu, and J. C. Kim, Development of new alumina-modified sorbents for $CO_2$

sorption and regeneration at temperatures below 200℃, Fuel, 2011, 90(4), 1465–1470.

[10] M. E$_L$-Merraoui, H. Tamai, H. Yasuda, T. Kanata, J. Mondori, K. Nadai, K. Kaneko, Pore structures of activated carbon fibers from organometallics / pitch composites by nitrogen adsorption, Carbon, 1998, 36(12), 1769-1776.

[11] D. A. Green, B. S. Turk, J. W. Portzer, R. P. Gupta, W. J. McMichael, Y. Liang, T. Moore, and D. P. Harrison, Carbon dioxide capture from flue gas using dry regenerable sorbents, Quarterly Technical Progress Report, 2003.

[12] R. W. Pekala and C. T. Alviso, Carbon aerogels and xerogels, Material Research Society Symposium process, 1992, 270, 3–14.

[13] W. Shen, S. Zhang, Y. He, J. Li, and W. Fan, Hierarchical porous polyacrylonitrile-based activated carbon fibers for $CO_2$ capture, Journal of Materials Chemistry, 2011, 21, 14036-14040.

[14] N. Díez, P. Álvarez, M. Granda, C. Blanco, R. Santamaría, R. Menéndez, $CO_2$ adsorption capacity and kinetics in nitrogen-enriched activated carbon fibers prepared by different methods, Chemical Engineering Journal, 2015, 281, 704-712.

[15] B. C. Bai, E. A. Kim, C. W. Lee, Y-S. Lee, J. S. Im, Effects of surface chemical properties of activated carbon fibers modified by liquid oxidation for $CO_2$ adsorption, Applied Surface Science, 2015, 353, 158-164.

# Chapter 5: General conclusion

$CO_2$ capture and storage is an agent problem has to be resolved in the near future, just like the prediction which detail described in chapter 1, the $CO_2$ emission result from human activities will change the environment dramatically. So in this study, we want to find a way that possesses a high $CO_2$ capacity and economic efficiency. $CO_2$ adsorption is closely associated with the properties of the porous material, we focus on the change of characterization of carbon aerogel by adjusting the ratio in the preparation process and impregnating $K_2CO_3$ nanocrystals into the mesopores of three CAs with different pore sizes of 7, 16, and 18 nm for the development of an excellent $CO_2$ sorbent with a high capacity, high selectivity, and low energy cost for regeneration. The performance of the nanocomposites is attributed to both chemical and physical capture being involved in the $CO_2$ capture. In chapter 3 from TG-DTA data that the $x$CA–KCs can be completely regenerated at temperatures below 423 K, 7CA–$K_2CO_3$ in particular exhibited excellent results, where regeneration began at 380 K and was completed at 420 K. These results were attributed to the high reactivity of nanostructured $K_2CO_3$, which rendered the $K_2CO_3$ crystals unstable and reduced the regeneration temperature. These $x$CA–KC nanocomposites exhibited excellent $CO_2$ capture capacity, 13.0, 9.77, 9.18 mmol $CO_2$/g $K_2CO_3$ for 7CA-$K_2CO_3$, 16CA-$K_2CO_3$, 18CA-$K_2CO_3$ composites, which all surpassed the theoretical value, respectively. We also concluded that CAs can be used as a porous support for the preparation of nanocomposites with low sorbent regeneration temperatures.

In chapter 4, we discussed the composite of impregnating the $K_2CO_3$ into the ACF-W15, which possess high surface area and pore volume, chemical inertness, and good mechanical stability. Even though ACF-KC also presented low regeneration

temperature, it still higher than 7CA-$K_2CO_3$ who regenerated at 380K, and did not get a higher $CO_2$ capacity compare to 7CA-$K_2CO_3$ by TG-DTA experiment.

The property of possessing micropore play an important role in increasing $CO_2$ capacity and reducing regeneration temperature, so we think maybe it is possible to decrease the pore size to more smaller than 7nm, getting a promising result in the future study. And in order to enhance the $CO_2$ capture amount, we think it is important to increase the loading amount of $K_2CO_3$ in the preparation process. There are still other aspects we have to consider such as maintain the adsorption capacity in the process of recycling, with the result of desorption / adsorption, we found that the $K_2CO_3$ sintering contributed to the inefficiency of xCA-KC composites, so we think this problem may be avoided by separating $K_2CO_3$ by smaller pore size in the further study.

# Appendix

| samples | Loading amount | C (T) | R(T) | $A_C$ | Conditions | Method | Reference |
|---|---|---|---|---|---|---|---|
| AC-K₂CO₃ | 30 | 333 | >473 | 86.3 | 1vol.%CO₂,9vol%H₂O,1atm | Fixed bed | [1] |
|  | 12.49 | 293 | 473 | 38.3 | 5000pmCO₂,1.8%H₂O,1atm | Fixed bed | [3] |
|  | 30 | 333 | >403 | 86.0 | 1vol% CO₂, 9vol% H₂O,1atm | Fixed bed | [6] |
|  | 26.4 | 363 | 433 | 46 | 11.8vol% CO₂,10vol %H₂O | Fixed bed | [15] |
|  | 35.9 | 333 | 473 | 99.4 | 15vol%H₂O,15vol%CO₂ | Fluidized bed | [16] |
| Al₂CO₃-K₂CO₃ | 30 | 333 | 623 | 89.0 | 1vol.% CO₂, 9vol%H₂O,1atm | Fixed bed | [1] |
|  | 28.5 | 293 | 623 | 51.9 | 5000pmCO₂, 1.8%H₂O,1atm | Fixed bed | [3] |
|  | 30 | 333 | 673 | 85.0 | 1vol% CO₂,9vol% H₂O | Fixed bed | [6] |
|  | 12.8-36.8 | 333 | 623 | 41-107 | 10vol% CO₂, 14 vol% H₂O | Fluidized bed | [11] |
|  | 60 | 333 | 473 | 128 | 1vol%CO₂,9vol%H₂O | Fixed bed | [12] |
| TiO₂-K₂CO₃ | 30.4 | 333 | 473 | 81.8 | 15vol%CO₂, 15vol%H₂O | Fluidized bed | [16] |
|  | 30 | 333 | 423 | 87 | 1vol.% CO₂, 9vol%H₂O,1atm | Fixed bed | [1] |
|  | 30 | 333 | >403 | 83.0 | 1vol% CO₂, 9vol% H₂O | Fixed bed | [6] |
|  | 30 | 333 | 473 | 90.0 | 1vol%CO₂, 9vol% H₂O | Fixed bed | [8] |

| samples | Loading | C (T) | R(T) | $A_c$ | Conditions | Method | Reference |
|---|---|---|---|---|---|---|---|
| αAl₂CO₃-K₂CO₃ | 30 | 333 | 473 | 95 | 1vol%CO₂,9vol%H₂O | Fixed bed | [17] |
| ZrO₂-K₂CO₃ | 30 | 333 | 473 | 76.3 | 1vol.% CO₂, 9vol%H₂O,1atm | Fixed bed | [1] |
|  | 30 | 323 | 423 | 91.6 | 1vol% CO₂, 9vol% H₂O | Fixed bed | [5] |
| MgO-K₂CO₃ | 30 | 323 | >623 | 178.6 | 1vol.%CO₂,11vol%H₂O,1atm | Fixed bed | [1] |
|  | 30 | 323 | >623 | 197.6 | 1vol.%CO₂,11vol%H₂O,1atm | Fixed bed | [2] |
|  | 30 | 333 | >623 | 119.0 | 1vol% CO₂,9vol% H₂O | Fixed bed | [6] |
| CaO-K₂CO₃ | 30 | 333 | >473 | 49.0 | 1vol.% CO₂, 9vol%H₂O,1atm | Fixed bed | [1][6] |
| SiO₂-K₂CO₃ | 30 | 333 | >473 | 10.3 | 1vol.% CO₂, 9vol%H₂O,1atm | Fixed bed | [1] |
| 5A-K₂CO₃ | 11.2 | 293 | 623 | 15.0 | 5000ppmCO₂,1.8%H₂O,1atm | Fixed bed | [3] |
| 13X-K₂CO₃ | 16.2 | 293 | 473 | 23.3 | 5000ppmCO₂,1.8%H₂O,1atm | Fixed bed | [3] |
| SG-K₂CO₃ | 37.5 | 293 | 473 | 6.6 | 5000ppmCO₂,1.8%H₂O,1atm | Fixed bed | [3] |
| K₂CO₃-MgO-Al₂O₃ | Al:30, Mg:10 | 333 | 753 | 109..6 | 10 vol% CO₂,12vol%H₂O, 78vol%air | Fluidized bed | [4] |
| USY-K₂CO₃ | 30 | 333 | – | 18.9 | 1vol%CO₂, 9vol% H₂O | Fixed bed | [6] |
| CsNaX-K₂CO₃ | 30 | 333 | – | 59.4 | 1vol%CO₂, 9vol% H₂O | Fixed bed | [6] |

| samples | Loading | C (T) | R(T) | A$_C$ | Conditions | Method | Reference |
|---|---|---|---|---|---|---|---|
| SiO$_2$-K$_2$CO$_3$ | 30 | 333 | – | 10.3 | 1vol% CO$_2$, 9vol%H$_2$O | Fixed bed | [6] |
| CNF-K$_2$CO$_3$ | 16-29 | 373 | 423 | 52.8-70.4 | 5vol% CO$_2$, 12vol%H$_2$O | Quartz plug-flow | [7] |
| Sorb KX35 | 35 | 343 | 503 | 90.0 | 14.4vol %CO$_2$,7vol %H$_2$O | Fluidized bed | [9] |
| | 35 | 333 | 473 | – | 10vol%CO$_2$,12.2vol H$_2$O | Fluidized bed | [10] |
| K$_2$CO$_3$-FeOOH | 33.33 | 333 | 398 | 49 | 1vol%CO$_2$, 10vol%H$_2$O, | Fixed bed | [13] |
| TiO$_2$-doped K$_2$CO$_3$/Al$_2$O$_3$ | Ti:3, K:36.8 | 333 | 473 | 101-109 | 10vol%CO$_2$, 12vol%H$_2$O | Fluidized bed | [14] |
| Y$_2$O$_3$-K$_2$CO$_3$ | 26.2 | - | 423-523 | 28 | In the air | - | [15] |
| Li4SiO4-K2CO3 | 30 | 853 | 973 | 230 | 4vol%CO$_2$, 96vol%N$_2$ | TG-DTA | [16] |

A$_C$: CO$_2$ capture capacity (CO$_2$ mg/g sorbent)

R (T): Regeneration temperature          C (T): Carbonation temperature

# References

[1] S. C. Lee, J. C. Kim, Dry potassium-based sorbents for $CO_2$ capture. Catalysis Surveys from Asia, 2007, 11, 171-185.

[2] S. C. Lee, H. J. Chae, S. J. Lee, B. Y. Choi, C.K.Yi, J. B. Lee, C.K. Ryu, J. C. Kim, Development of regenerable MgO-based sorbent promoted with $K_2CO_3$ for $CO_2$ capture at low temperatures, Environmental Science & Technology, 2008, 42, 2736-2741.

[3] C. Zhao, Y. Guo, C. Li, S.Lu, Removal of low concentration $CO_2$ at ambient temperature using several potassium-based sorbents, Applied Energy, 2014, 124, 241-247.

[4] L. Li, Y. Li, X. Wen, F. Wang, N. Zhao, F. Xiao, W. Wei, Y. Sun, $CO_2$ capture over $K_2CO_3/MgO/Al_2O_3$ dry sorbent in a fluidized bed, Energy &Fuels, 2011, 25, 3835-3842.

[5] S. C. Lee, H. J. Chae, S. J. Lee, Novel regenerable potassium-based dry sorbents for $CO_2$ capture at low temperatures, Journal of Molecular Catalysis B: Enzymatic, 2009, 56, 179-184.

[6] S. C. Lee, B. Y. Choi, T. J. Lee, C. K. Ryu, Y. S. Ahn, J. C. Kim, $CO_2$ absorption and regeneration of alkali metal-based solid sorbents, Catalysis Today, 2006, 111, 385-390.

[7] N. N. A. H. Meis, A. M. Frey, J. H. Bitter, K. P. de Jong, Carbon nanofiber-supported $K_2CO_3$ as an efficient low-temperature regenerable $CO_2$ sorbent for post-combustion capture, Industrial & Engineering Chemistry Research, 2013, 12812-12818.

[8] S. C. Lee, Y. M. Kwon, Y. H. Park, W. S. Lee, J. J. Park, C. K. Ryu, C. K. Yi, J. C. Kim, Structure effects of potassium-based $TiO_2$ sorbents on the $CO_2$ capture capacity, Topics in Catalysis, 2010, 53, 641-647.

[9] C−K. Yi, S−H. Jo, Y. Seo, J−B. Lee, C−K Ryu, Continuous operation of the potassium-based dry sorbent $CO_2$ capture process with two fluidized-bed reactors, International Journal of Greenhouse Gas Control, 2007, 1(1), 31−36.

[10] Y. Seo, S. H. Jo, H. J. Ryu, D. H. Bae, C. K. Ryu, C. K. Yi, Effect of water pretreatment on $CO_2$ capture using a potassium-based solid sorbent in a bubbling fluidized bed reactor, Korean Journal of Chemical Engineering, 2007, 24(3), 457-460.

[11] C. Zhao, X. Chen, C. Zhao, Y. Wu, W. Dong, $K_2CO_3/Al_2O_3$ for Capturing $CO_2$ in Flue Gas from Power Plants. Part 3:$CO_2$ Capture Behaviors of $K_2CO_3/Al_2O_3$ in a Bubbling Fluidized-Bed Reactor, Energy fuels, 2012, 26, 3062-3068.

[12] S. C. Lee, Y. M. Kwon, C. Y. Ryu, H. J. Chae, D. Ragupathy, S. Y. Jung, J. B. Lee, C. K. Ryu, J. C .Kim, Development of new alumina-modified sorbents for $CO_2$ sorption and regeneration at temperatures below $200^0C$, Fuel, 2011, 90, 1465-1470.

[13] B−T. Zhang, M. Fan, A. E. Bland, $CO_2$ separation by a new solid K-Fe sorbent. Energy Fuels, 2011, 25, 1919-1925.

[14] W. Dong, X. Chen, Y. Wu, $TiO_2$-Doped $K_2CO_3/Al_2CO_3$ sorbents for $CO_2$ capture, Energy Fuels, 2014, 28, 3310-3316.

[15] V. S. Derevschikov, J. V. Veselovskaya, T. Y. Kardash, D. A. Trubitsyn, A. G. Okunev, Direct $CO_2$ capture from ambient air using $K_2CO_3/$ $Y_2O_3$ composite sorbent, Fuel, 2014, 127, 212-218.

[16] M. Seggiani, M. Puccini, S. Vitolo, Alkali promoted lithium orthosilicate for CO2 capture at high temperature and low concentration, International Journal of Greenhouse Gas Control, 2013, 17, 25-31.

## Acknowledgements

First and foremost I would like to express my deepest gratitude to my advisor Professor Hirofumi Kanoh, for his invaluable guidance, consistent encouragement, and support. I learned many qualities from him, such as dedication, optimism, care to students who may have a dilemma in their research or life. I also became more enthusiastic in doing my research, learning professional knowledge, improving language skills, and helping other people. I wish to express my deep and sincere gratitude to Associate professor Tomonori Ohba for the precious comments and invaluable discussion. I want to thanks Mr. Ohazama who has taught me about how to use Belsorp to measure $CO_2$ adsorption and data analysis, Mr. Okuno who always help me when I have troubles in my research like device damage, assemble instrument, and Mr. Yamamoto who spend much time to teach me about how to use the water line.

I would like to thank all members of Molecular Chemistry group & Molecular Nanochemistry group of Chiba University for being important in my study and life. During this work, their supports and encourages have been very helpful in my research activities and make me feel part of their warm family. Thanks to all for your helps and kindness during my stay in Japan and teaching me about hard work, respectful and many other good values.

Finally, I would like to thank my family for great understanding, encouragement and support in my life and study.

February, 2016

Guang Yang